Episodic growth of fold-thrust belts: insights from Finite Element Modelling

Xiaodong YANG [a,*], Frank J. PEEL [b,c], David J. SANDERSON [a,d], Lisa C. McNeill [a]

[a] Ocean and Earth Science, National Oceanography Centre, Southampton, University of Southampton, Southampton, SO14 3ZH, UK.

[b] Department of Earth Science and Engineering, Imperial College London, London, SW7 2BP, UK.

[c] Bureau of Economic Geology, The University of Texas at Austin, Austin, TX, USA.

[d] Engineering and Environment, University of Southampton, Southampton, SO17 1BJ, UK.

* Corresponding author, email: xy3g14@soton.ac.uk, telephone: +44(0)2380596020

Key words: Thrust wedge, Fold-thrust belt growth, Critical taper, FEM modelling.

Abstract

The sequential development of a fold-thrust belt was investigated using 2D Finite Element Modelling (FEM). The new model results show that a thrust system is typically composed of three distinct regions: the thrust wedge, pre-wedge, and undeformed region. The thrust wedge involves growth that repeats episodically and cyclically. A cycle of wedge building starts as frontal accretion occurs, which is accompanied by a rapid increase in wedge width reducing the taper angle below critical. In response to this, the wedge interior (tracked here by the 50 m displacement position) rapidly propagates forwards into a region of incipient folding. The taper angle progressively increases until it obtains a constant apparent critical value (~10°). During this period, the wedge experiences significant shortening after a new thrust initiates at the failure front, leading to a decrease in wedge width. Successive widening of the wedge and subsequent shortening and thrusting maintain a reasonably constant taper angle. The fold-thrust belt evolves cyclically, through a combination of rapid advancement of the wedge and subsequent gradual, slow wedge growth. The new model results also highlights that there is clear, although minor, deformation (0-10 m horizontal displacement) in front of the thrust wedge.

1. Introduction

The Coulomb Wedge Model (CWM) has been very successful in describing the mechanics of orogenic and subduction-related thin-skinned fold-thrust belts from around the world (Davis et al., 1983; Dahlen, 1984; Dahlen et al., 1984; Platt, 1986; Zhao et al., 1986; Lallemand and Le Pichon, 1987; Woodward, 1987; Dahlen, 1990; Braathen et al., 1999; Mouthereau et al., 2006; Suppe, 2007; Fagereng, 2011; von Hagke et al., 2014; Sun et al., 2016). According to the model, the thrust belt is analogous to a wedge of soil or snow in

front of a moving bulldozer, and the material within the wedge deforms until it develops a critical taper, and basal shear and wedge translation can occur (internal and basal shear stresses are balanced in critical state), after which it grows self-similarly as additional material is accreted at the toe (Davis et al., 1983; Dahlen, 1984; Dahlen et al., 1984; Dahlen, 1990). The theory can be used to understand the effects of internal and basal strength (Mulugeta, 1988; Willett, 1992; Burbidge and Braun, 2002; Lohrmann et al., 2003; Simpson, 2009), dip of detachment (Davis et al., 1983; Koyi and Vendeville, 2003; Smit et al., 2003), surface slope and topography (Marques and Cobbold, 2002, 2006; Sun et al., 2016), lateral friction (Zhou et al., 2016), surface processes, i.e., erosion and sedimentation (Storti and McClay, 1995; Hoth et al., 2006; Simpson, 2006; Stockmal, 2007; Cruz et al., 2010; Simpson, 2010a; Wu and McClay, 2011; Fillon et al., 2012), and the rheology of single and multiple detachments (Ruh et al., 2012) on the growth of fold-thrust belts. For a review see Buiter (2012) and Graveleau et al. (2012).

Coulomb Wedge Model only provides a static view of the thrust wedge, assuming constant conditions with the wedge maintained at Coulomb failure throughout (Chapple, 1978; Davis et al., 1983). A simple Coulomb Wedge retains a constant taper as it moves without addition of material being encountered (Fig. 1a, see Supplementary Material). In reality, as a wedge grows, new material is added, most commonly at the toe (Fig. 1b), with the thrust wedge accreting in a piggyback style during its forward advance (Mulugeta and Koyi, 1992). Accommodated by nucleation of new thrusts in front of the wedge, accretion of sediments thickens the wedge and raises the surface topography (Platt, 1986; Mulugeta and Koyi, 1992; Gutscher et al., 1996; Burbidge and Braun, 2002; McClay et al., 2004; Bigi et al., 2010), rendering the wedge unstable. A stable geometry can be regained by internal deformation, most commonly involving shortening, imbricating and folding (Fig. 1c; Davis et

al., 1983; Lallemand and Le Pichon, 1987; Burbidge and Braun, 2002). As real world thrust wedges develop, they do so by the addition of discrete, often large, thrust sheets (Fig. 1d). Evolution of the wedge taper angle occurs by progressive internal deformation and accretion of new units to the wedge front (Fig. 1c). The initiation of discrete faults or zones of deformation produces an episodic development (Fig. 1d), with a change in shape and taper angle as the wedge grows. Accretion of new material into the wedge may not occur at the same time as deformation within the wedge. This behaviour is seen in physical analogues, with the wedge geometry changing as the accretion of imbricate slices builds the wedge forward, thereby lowering the taper to subcritical (Gutscher et al., 1996; Lohrmann et al., 2003). The assumption that thrust wedges constantly exist in a state of critical taper is therefore not sufficient to describe the dynamic evolution of a real thrust wedge.

In natural systems, a number of studies of the growth of fold-thrust belts have been undertaken. Fitz-Diaz et al. (2014) used illite Ar/Ar dating to obtain absolute ages of folds and shear zones, suggesting episodic progression of deformation from west to east in Mexican Fold-Thrust Belt. Through detailed chronostratigraphic study of syn-tectonic sediments, the episodic uplift of mountain ranges (Ji et al., 2008; Lease et al., 2012) and growth of an individual anticline(Masaferro et al., 1999) have been reported. Studies of the deep-sea turbidites and silicic plutonic sequences revealed the episodic growth of the south-west Alaska convergent margin (Byrne and Fisher, 1987). Though these field-based studies reveal the overall growth pattern of mountain belt and accretionary prism, the quantitative spatial and temporal variations in associated geometric parameters are still poorly resolved. For example, what is the behaviour of wedge material when transported forwards? Is deformation constant or episodic? What are the effects of thrust initiation and frontal accretion on wedge geometry? What happens in front of the wedge when

developing a critical taper? How do these different elements correlate with each other during the wedge-building process?

Numerical modelling and scaled analogue experiments with digital image correlation technique can provide insights into the dynamic evolution of deforming wedges because these enable us to simulate the development of a realistic thrust system, and to measure the geometry, stress, and strain at every stage in its growth, which cannot be done for natural examples (Beaumont et al., 1992; Ellis et al., 2004; Adam et al., 2005; Buiter et al., 2006; Simpson, 2006; Yamada et al., 2006; Selzer et al., 2007; Stockmal, 2007; Selzer et al., 2008; Simpson, 2009; Cruz et al., 2010; Simpson, 2010b; Buiter, 2012; Fillon et al., 2012; Ruh et al., 2012; Adam et al., 2013; Ruh et al., 2013; Buiter et al., 2016; Dotare et al., 2016).

This study aims to produce a 2D finite element model (FEM), built with Abaqus 6.14, to investigate the dynamic growth of a simple fold-thrust belt that includes frontal accretion at the wedge toe. This model is used to understand:

(1) How the system propagates at the wedge toe and quantify what happens in front of the thrust wedge.
(2) How the critical taper is achieved in response to wedge accretion, testing this against the theoretical predictions from the CWM (Dahlen, 1984). How the spatial and temporal evolution of different variables can be resolved during the critical-subcritical transition period.
(3) How the thrust system evolves over many cycles of wedge building in terms of internal wedge movement, propagation of displacement front and failure front, and variations in wedge height and width.

2. Models

2.1. Brittle rheology and material properties

The wedge is modelled as a mass of homogeneous, cohesive material whose behaviour is visco-elasto-plastic resembling that of dry quartz sand (Table 1). The material deforms elastically until plastic or viscous yield is reached, after which deformation continues on yield (Buiter et al., 2006). It is therefore equivalent to physical analogue (sandbox) models that themselves constitute scaled models of natural systems. The mechanical parameters assigned to the model are density, Young's modulus, Poisson's ratio, internal friction angle and basal friction angle, Poisson's ratio, gravity, angle of dilation, cohesion and viscosity, with values taken from previous studies(Ellis et al., 2004; Buiter et al., 2006) (see Table 1). The wedge material deforms elastically at the early stage after loading and shortening, followed by strain hardening prior to failure at peak strength (Lohrmann et al., 2003). Further strain leads to softening until the stable dynamic strength is reached (Lohrmann et al., 2003; Panien et al., 2006). The Drucker-Prager failure criterion is employed as a smooth version of the angular Mohr-Coulomb failure criterion to model the wedge deformation (Buiter, 2012; Tuitt et al., 2012). Localised failure in the form of shear bands occurs close to the peak strength at maximum dilation rates, whereas the dynamic stable state is associated with decreased dilation rates (Buiter et al., 2016). The dynamic stable state is a stage characterised by a dynamically constant shear load and steadily increasing shear strain. Strain softening is simulated by a linear decrease from a peak internal friction angle to a stable frictional angle over a finite strain interval of 0.5-1.0 (finite strain is total accumulated effective strain as measured by the square root of the second invariant of the strain tensor) (Buiter et al., 2006). A frictional contact is implemented between the wedge

and wall and base. Gravity is applied as a distributed load on the wedge material. Since the code models frictional behaviour using a Coulomb yield criterion with non-associated flow law, frictional volumetric changes (or dilation) are not included in the model.

Discrete faulting (movement on a fault surface) cannot be modelled as the solution does not support the development of discontinuities in the mesh. The FE solution, together with the strain-softening rheology, results in the development of narrow shear zones which effectively behave as discrete faults at a macroscopic scale. The computational mesh grids are sufficiently fine to model movement on these zones, with elements up to a maximum aspect ratio of ~15. Re-meshing was tried, but did not significantly improve the modelling of these shear bands.

2.2. Model set-up

Our model is a two-dimensional representation of a propagating thrust system. As a simple test of the model and its parameters, we reproduced a simple experiment of Buiter et al. (2016), in which a wedge of material is moved over a horizontal base with no frontal accretion (i.e., Fig. 1a). The model results are described in the Supplementary Material and demonstrate that Abaqus can model a simple thrust wedge, maintaining its initial taper angle (20°) after 1500 m of translation, in accordance with the CWM (Davis et al., 1983) .

Other model tests (see Supplementary Material) were used to explore the solution sensitivity to changes in the following parameter values: strain-softening thresholds, material strength, initial wedge thickness and mesh resolution (cell size). The results mainly indicate the strain-softening exerts a first order control on strain localisation, the mesh size determines the width of shear zone while the thickness of the initial model governs the fault spacing.

In this study, we accept the observations describing general thrust system development, and its sensitivity to controlling parameters. These have been established by previous publications, and we take these as a starting point. The model presented in the main body of this paper does not include a full parameter study of the whole system. We focused on a model with parameters similar to Buiter et al. (2006). Our FEM does not include re-meshing, so we present results from the model that remained numerically stable to the largest increment of shortening. We use this to investigate in detail the important aspects of thrust development that are revealed by systematic fine-scale analysis. Our focus was particularly directed at the spatial and temporal variation in the earliest stages of thrust fault propagation, which are revealed by examining the first increments of displacement and strain, particularly in the frontal regions of the developing thrust wedge.

We constructed the main model (Fig. 2a) as a wedge with an initial horizontal surface (i.e. with a subcritical taper). It consists of a mobile left-hand wall, a fixed right-hand wall and base, containing a body of homogenous, isotropic sediment length 10000 m and initial thickness 600 m (Fig. 2a), with passive, initially horizontal marker layers. The size of the FE cell is 25m X 25m, with a total of 9600 cells set up to model the thrust deformation, providing adequate detail/resolution to examine the wedge dynamics. The model thickness of 600 m is chosen to be more realistic for the toe of a real wedge. Abaqus can only handle small-scale deformation: we tested a number of models with various size, and the one with dimension 10000 m x 600 m gives the most geological reasonable results, and allows computation of largest horizontal displacement (3268m). Shortening is modelled by moving the mobile wall from left to right whilst the right wall and base remain fixed. The moving wall is in direct contact with the base, therefore a sharp velocity discontinuity is formed at the left corner (Buiter et al., 2016), which affects the initial development of the thrust

wedge. The coefficient of effective friction between the walls and the horizontal layers is 0.075, and the coefficient of friction between the horizontal layers and base is 0.3. The basal friction should not exceed the internal friction for the existence of Coulomb Wedge, and an even smaller side friction allows the wedge material to move freely along the walls.

We selected this model (including the side friction 0.75 and basal friction 0.3) based on the following requirements:

(1) To generate the geologically reasonable results (looks like the natural examples and experimental models);

(2) To use parameter values based on those used in previous studies (and often remain the same), permitting direct comparison between our results and other studies.

(3) To enable computation of the largest displacement, allowing us to derive the maximum value from the simulation.

The system is described by a fixed 2D coordinate system in which the origin (x=0, y=0) is defined as the position at the bottom left corner at the start of model (Fig. 2a).

2.3. Thrust Belt Model

The main model was set up 1) to allow building of a critically tapered wedge from the horizontal layers and then 2) to investigate how the subsequent thrust wedge develops and accretes material. The spatial positions within the wedge and associated deformation parameters are specified in relation to a 2D coordinate system which has a fixed zero position at the initial base of the vertical wall (Fig. 2a). Key geometrical parameters of the thrust system are systematically measured and analysed in order to investigate the quantitative growth of the fold-thrust belt (Figs. 2b & 2c). These are:

a) Displacement front - the point of zero displacement along the detachment which shows

how far shortening is transmitted across the deforming wedge along its base, the parameter positions tracked for analysis are all horizontal displacements;

b) *50 m displacement* position–we constantly tracked the point at which a fixed and relatively small displacement (50 m) is reached along the basal detachment. This is used to track the development of displacement behind the displacement front (i.e., in front of the main thrust wedge). The selection of a 50 m-offset threshold is somewhat arbitrary, but it (1) lies within the range of displacements accumulated during a cycle; (2) the point of 50 m displacement is consistently ahead of the new frontal thrust, but it sufficiently far from the displacement front to illustrate the cyclic changes; and (3) ends up within the strain gradient that localises into the next frontal thrust. Following the position of a fixed amount of displacement provides a useful insight into the cyclic evolution of the thrust system and a valuable and instructive marker of minor deformation;

c) *Failure front* – the point at which the current frontal thrust fault roots into the detachment. This is of particular importance for understanding the initiation and forward advancement of a new thrust fault (Fig. 2b);

d) *Surface deformation front* – the point of zero displacement at the surface;

e) *Inboard corner* of the wedge - used to examine how a critical taper is developed and reached (Fig 2b);

f) *Taper angle* - determined by the slope of the straight line from the deformation front *d* to the inboard corner of the wedge *e;*

g) *Surface slope* - determined as the best fitting line enveloping the thrust wedge (i.e., Bigi et al., 2010; Schreurs et al., 2016; see also Fig. 2c);

h) Wedge height - the highest elevation of the top of thrust wedge (Fig. 2c);

w) Wedge width - measured as the horizontal distance from the deformation front *d* to the moving left-hand wall.

The locations of the measured parameters are shown graphically by their x-coordinates, measured from the initial left hand side of the model (Fig. 2).

3. Results

After experimentation with a range of input parameters, we ran a number of models, which show very similar features but with some differences observed (see Supplementary Material). Here we describe results for a single model that provided the longest "well-behaved" numerical simulation with no computational problems and fits the requirements described in Section 2.2 above for most feasible parameter values (Fig. 3). The total shortening of the model is 3268 m, with all geometric parameters measured at every 17-67 m of shortening, the exact value being determined by the stepped nature of the numerical solution.

At the final stage of the simulation, six major thrust faults developed (F1 – F6), dividing the model into six imbricate fault blocks (*I*1 to *I*6) and a less deformed footwall block with minor folding (Fig. 4). The first group of faults F1-F3 are located close to the moving left hand wall: they initially develop from the detachment, they are subsequently squeezed and rotated by both the mobile wall and velocity discontinuity at the left corner (Buiter et al., 2016). These form an initial wedge with shortening resulting in 3 closely-spaced thrusts (~200 m apart, see Stage 1 in Fig. 3). In contrast, in the second stage of wedge development, faults F4 to F6 develop and propagate forward away from the model boundary with a wider

fault spacing of 940 -1400 m (see Stage 2 in Fig. 3). Two short-cut faults (red dotted lines, Fig. 4) are created within the imbricate blocks *I*4 and *I*6, which lead to connection between F3 and F4, and F5 and F6 (Figs. 3 & 4).

Details of the shear zone grid are shown in Figure 3. The cell is significantly deformed and elongated along the shear zone and tilted towards the foreland. The geometry of deformed numerical cell is similar to that observed from numerical models and scaled analogue experiments (Ellis et al., 2004; Adam et al., 2005). In contrast, the cells at the region away from the shear zones show little deformation, in accordance with the implemented Mohr-Coulomb failure criterion.

The fold-thrust system can be divided into three regions (Fig. 4):

i. The thrust wedge, which consists of the material above and behind the frontal imbricate thrust;

ii. The pre-wedge, ahead of the frontal imbricate thrust, in which strain builds up as a gentle fold and some lateral translation due to movement on the basal detachment. This region is similar (but not equivalent) to the previously recognised "proto-thrust" region in sub-marine accretionary prisms (Karig and Lundberg, 1990; Tsuji et al., 2005; Ku and Hsu, 2009; Lin et al., 2009; Barnes et al., 2010; Ghisetti et al., 2016) as both regions deform the present-day seafloor and tend to be incorporated into the main deforming wedge as deformation proceeds. However the proto-thrust region described by these authors commonly contains sets of moderately to steeply dipping reverse faults, and has been identified as the region both ahead (MacKay, 1995; Moore et al., 2001; Gulick et al., 2004; Ku and Hsu, 2009; Barnes et al., 2010; Ghisetti et al., 2016) and behind (Adam et al., 2004; Ku and Hsu, 2009; Lin et al., 2009) the deformation front. However, the pre-wedge in our model is characterised by gentle

detachment folding without major established faults, and is situated between the frontal thrust and deformation front (Fig 4). The proto-thrust described by Karig and Lundberg (1990) and others is a qualitative definition. In contrast, we can define the pre-wedge region by the quantified wedge features, i.e., displacement front, deformation front and failure front (Fig. 4);

iii. The undeformed region, ahead of the displacement front, with the boundary between the pre-wedge region and undeformed zone being diffuse, as displayed by the dotted line in Figure 4.

3.1. Surface slope and taper angle

One of the primary applications of the CWM is to predict the critical taper angle of a thrust belt by combining the known or estimated rock strength and stress equilibrium conditions within the wedge interior and along the basal detachment (Davis et al., 1983; Dahlen, 1984, 1990). Here we can test whether the taper angle of the modelled thrust wedge is consistent with these theoretical predictions.

As shortening is applied to the moving wall, the surface slope starts to grow rapidly until it reaches an angle of 24.8°, at ~413 m shortening (Fig. 5). It then increases slowly to a peak value of 25.4°, at ~750 m shortening, at which, the slope angle then rapidly decreases to 13.0° . Similar to the surface slope, the taper angle exhibits an initial increase to a peak value of 16.4° (Fig. 5). Within this first fast growth phase, there are two brief periods where the taper angle is relatively stable; from 165 m to 228 m of shortening, and 367 m to 413 m of shortening. These two episodes represent the rapid transitional process from critical to sub-critical state of the thrust wedge. Following ~700 m shortening, the taper angle decreases from 16.5° to 10.4° (as the surface slope decreases from 25.4° to 13.0°).

These results indicate that the model can be divided into two time stages:

1) Stage 1: A period (from 0 – 700 m shortening) in which a wedge is built adjacent to the moving wall. At this stage the failure front is fixed at the origin and the wedge gains height and topography through the development of fault blocks *I*1, *I*2 and *I*3 (Figs. 4 & 5). Up to this point there is little deformation ahead of the wedge, with the 50 m shortening extending to ~700 m (Fig. 3). During this stage, the geometry of the model is largely controlled by the boundary conditions, particularly of the moving wall and velocity discontinuity at the left corner and may not be indicative of natural thrust belts. This stage does not represent the critical taper relationship and is not used in our detailed analysis.
2) Stage 2: Beyond 700 m shortening, the system transitions rapidly into a dynamic equilibrium state. During this stage there is oscillation between critical and sub-critical taper, with both surface slope and taper angle having a constant apparent critical value of ~10°. This stage is characterized by an approximately steady state development of thrust wedges *I*4, *I*5 and *I*6, and will be discussed in detail in the rest of the paper as it is thought to be highly relevant to natural thrust systems.

Figure 5 shows that the surface slope is consistently larger than the simplified taper angle in the early period of establishing the thrust wedge (before shortening of 1110 m). With the exception of differences in values at the initial wedge development stage, the evolution patterns of surface slope and taper angle are very similar to each other. As the bulk strength is controlled by the weakest component of material friction strength (Lohrmann et al., 2003) which in this case is 31° (Table 1) , the minimum and maximum critical taper are computed as 5.8° and 31° using the solution of Dahlen (1984) (Fig. 1a, eq. 1-5). The wedge fails by thrusting at the minimum critical taper while failing by normal faulting at the maximum

critical taper. All measured surface slope and taper angles remain in the stable field of the Coulomb Wedge (Dahlen, 1984), similar to that observed from previous studies (Buiter et al., 2006; Schreurs et al., 2006; Cruz et al., 2010; Buiter et al., 2016), demonstrating the model results are effective. In this case, the thrust wedge is established through folding and thrusting as the modelled constant apparent critical value of surface slope and taper angle, both ~ 10°, is approaching the minimum critical taper angle 5.8° predicted by CMW (Dahlen, 1984).

$$\psi_b = \frac{1}{2}\arcsin\left(\frac{\sin\varphi'_b}{\sin\varphi}\right) - \frac{1}{2}\varphi'_b \quad (1)$$

$$\psi_0 = \frac{1}{2}\arcsin\left(\frac{\sin\alpha'}{\sin\varphi}\right) - \frac{1}{2}\alpha' \quad (2)$$

$$\varphi'_b = \arctan\left[\mu_b\left(\frac{1-\lambda_b}{1-\lambda}\right)\right] \quad (3)$$

$$\alpha' = \arctan\left[\left(\frac{1-\rho_w/\rho}{1-\lambda}\right)\tan\alpha\right] \quad (4)$$

$$\alpha_{max} = \arctan\left[\frac{\mu(1-\lambda)}{1-\rho_w/\rho}\right] \quad (5)$$

ψ_b and ψ_0 are the angles between the maximum principal compressive stress and base and top of the wedge, φ angle of internal friction (μ=tan φ), φ_b angle of basal friction (μ_b=tan φ_b), λ the pore fluid factor in wedge, λ_b basal pore fluid factor, ρ density of wedge material, ρ_w density of fluid.

The analytical CWM has been developed as a description of a static wedge in a condition of stress equilibrium and it does not incorporate the effects of discrete thrust and related folding on wedge growth. Real world thrust systems and modelled wedges evolve dynamically with imbricated thrusts and folds that affect the overall geometry of thrust wedge, which probably results in the inconsistency between theoretical and measured taper angles (pers. comm., J. Suppe, 2016). In addition, the definition of a single value for the

"taper angle" in real-world systems is non-trivial, because they commonly exhibit complex topography, and rarely consist of simple uniform-tapering wedges.

In this study, we define "taper angle" simply as the slope of the straight line from the deformation front to inboard corner of the wedge (Fig. 2b), which ignores any variation in topography of the top surface of the modelled thrust belt. Figure 5 shows how the overall taper angle of the model continuously changes as the model develops, with a tendency for it to self-adjust in such a way as to approach the minimum critical taper. This behaviour was also observed in physical analogue experiments by Wang and Davis (1986) and Lohrmann et al. (2003). In our numerical models, the constant critical taper angle appears to be approximately 10°. Taper angles below this value are subcritical, because they cannot be stably maintained. The frontal ramp (pre-wedge in Fig. 4), side friction, imposed boundary conditions, velocity discontinuity at the left corner (Fig. 2) and material cohesion all affect the modelled taper angle.

3.2. Wedge width and height

Wedge height and width are plotted against shortening (Fig. 6a), and separately as growth rate of wedge height (Fig. 6b). Wedge height is defined as the highest elevation of the top of thrust wedge, with the initial value of height being the original thickness of the pre-deformation thrust wedge (600 m; Fig. 2b). Its growth rate is the slope of wedge height calculated from two successive values of shortening. Wedge width is measured between the mobile wall and the deformation front (see Cotton and Koyi, 2000; Schreurs et al., 2006; Fig. 2b).

In our model, there are 6 distinct episodes of rapid increase in wedge width (Fig. 6a). In each episode, displacement steps forward along the basal decollement and a new incipient

fold develops. The rapid jumps in wedge width are followed by a slow increase and then decrease in wedge width prior to the next phase of wedge accretion. The second 'steady state' stage (Stage 2: shortening >700 m) follows a significant increase in wedge width (~900 m). An overall wedge width of 4650 m is gained over shortening of 3268 m. Such a phased accretion in the thrust wedge has also been reported by previous authors (Mulugeta and Koyi, 1992; Cotton and Koyi, 2000; Bigi et al., 2010; Cruz et al., 2010; Wu and McClay, 2011; Ruh et al., 2012).

In contrast, the wedge height continuously grows to 1025 m, at shortening of ~700 m (Fig. 6a), with growth rates of 0.5-0.8(Fig. 6b), and then increases more slowly until it reaches 1396 m at 3268 m of shortening (Fig. 6a), with a growth rate range of 0.0-0.3 (Fig. 6b). The episodes of rapid increase are less obvious, but there is some indication of cyclicity, in parallel with wedge accretion. Similar results have been observed in physical analogue models through direct measurement of wedge height (Koyi, 1995; Burbidge and Braun, 2002; Bose et al., 2009). Bose et al. (2009) reported that early rapid increasing wedge height is followed by a long-term stable wedge growth. Our results show wedge height continuous to grow with alternating high and low rates throughout the entire process. Potentially our model allows more detail to be resolved in this "stable" phase (Stage 2 in Fig. 6).

3.3. Propagation of the displacement front, 50 m displacement position and failure front

In the process of developing a thrust wedge, the material within the wedge is deformed by folding and faulting as the thrust wedge progressively advances into the undeformed frontal area (Wu and McClay, 2011). This episodic and cyclic growth pattern has been seen in sand box models (Mulugeta and Koyi, 1992; Willett, 1992; Gutscher et al., 1996; Wang and Davis, 1996; Gutscher et al., 1998; Sherkati et al., 2006; Selzer et al., 2008). In this study,

three parameters are used to show how a thrust belt evolves in response to continuous convergence: the displacement front; the 50 m displacement position; and the failure front (Figs. 2b & 2c).

The distribution of total, horizontal and vertical displacement for the model scaled to 0-2390 m, 0-2300 m and 0-665 m are displayed in Figures 7a, 7b & 7c, respectively. The total and horizontal displacement present similar patterns of distribution, indicating that the horizontal/forward movement dominates the growth of the thrust belt. However, the fully scaled models cannot resolve minor deformation (less than ~230 m) or the displacement front location (position of 0 m displacement) due to limited resolution. Therefore, we also plot at a different scale (0-50 m) to highlight small scale displacement and to constrain incipient deformation in the wedge front (Figs. 7d, 7e&7f). Because the system is dominated by forward advancement, the horizontal positions of the displacement front, the 50 m displacement and the failure front along the detachment are defined to examine the advancing behaviour of the wedge front (Fig. 7f).

In order to reveal the details of these displacement parameters, in each case the propagation rate of the parameter is calculated using the same method as that for the growth rate of wedge height (see above). The displacement front propagates forward at variable rates from a position of 540 m to 7880 m during the two stages of wedge building (Fig. 8). The propagation rate plot of this parameter (Fig. 8b) indicates cyclicity, with alternating high and low propagation rates with the latter relating directly to the cyclic changes in the wedge height (Fig. 6b).

The 50 m displacement position starts at a position of 119 m at shortening 84 m (Fig. 9). The position advances over 6 cycles each composed of a relatively long period of slow forward propagation followed by a short episode of rapid propagation. The first three of

these cycles are developed within Stage 1 and represent relatively small advancements of position and low propagation rates. These are followed by 3 further cycles within Stage 2 that include phases of high propagation rate and greater jumps forward in the position of the 50 m displacement within Stage 2.

The failure front initiates at a position of 154 m at shortening 84 m (Fig. 10). As with the 50 m displacement position, six cycles can be identified where relatively long periods of slow propagation are followed by rapid advancement. Rapid propagation of the failure front typically occurs as an old thrust is abandoned and a new thrust is about to initiate at the failure front. As soon as this happens, the newly formed thrust (and hence the failure front) then tends to advance very slowly (Fig. 10). pari

3.4. The spatial and temporal relationship between the displacement front, 50 m displacement and failure front

To investigate how the different deformation parameters are related, they are plotted together against shortening as a proxy for time (Fig. 11). In contrast to the episodic propagation of the 50 m displacement position and failure front, the displacement front shows a relatively constant advance (Fig. 11a), suggesting that this parameter is less affected by the wedge building process. The rapid propagation of the 50 m displacement position and failure front are not coincident in time, with the 50 m displacement position advancing before the failure front (Fig. 11). As displayed in Figure 11b, the rapid propagation of failure front (shown by orange line) lags behind that of the 50 m displacement position (shown by red line). The 50 m displacement position moves progressively forward before reaching a stable position, prior to the establishment of a new failure front. The deformation sweeps forward, and then stabilizes, with new failure front

then localising in the resulting displacement gradient. For example, in the development of wedge *I*4, the 50 m displacement position propagates to a new position with progressive shortening and then the failure front jumps to this position as a new discrete fault forms (Fig. 11a).

Figure 12 presents the data redisplayed in order to emphasize the spatial relationships. The graph tracks the position of three features: the displacement front, the 50 m displacement and the failure front. The separation of the 50 m displacement position from the displacement front provides a measure of the displacement gradient at the tip and following the position of this marker provides a useful insight into the cyclic evolution of the thrust system. Throughout the process of wedge building, the displacement front is leading the system in advance of both the 50 m displacement position and failure front (Fig. 12).

The key stages in the growth of a thrust wedge can be visualized from the modelling results (Fig. 13). Here, two sets of model images of horizontal displacement and distributed strain are used to illustrate the cyclic evolution of imbricate block *I*6 in Stage 2 as an example of the typical cycle of wedge growth. The strain used is principal strain derived from the FE modelling, which is indicative of the magnitude and distribution of deformation in a simulated thrust belt. Four stages are depicted, as follows:

1) ~2278 m (shortening), wedge accretion (start of a cycle). This phase is characterised by the rapid advancement of the 50 m displacement position towards the zone of incipient folding (Fig. 13a) while the frontal thrust is slowly advancing. A zone of minor strain occurs (Fig. 13e) highlighting the initial minor deformation corresponding to the observed minor displacement in the pre-wedge region.
2) ~2529 m, diffused deformation. With additional bulk shortening, the 50 m displacement position completes its rapid forward propagation as indicated by the narrow zone of

large displacement (red band in Fig. 13b). This is accompanied by the expansion of diffused deformation across the outermost area of folding (Fig. 13f), similar to the observed “diffuse shear strain” of Adam et al. (2005). These features are also compatible with the previously reported activity of numerous short-lived weak shear bands prior to the initiation of a new thrust in scaled analogue models (Dotare et al., 2016). At this point, the incipient fold is above a broad strain zone not a discrete thrust, and is therefore identified as a pre-thrust anticline.

3) ~2766 m, strain localisation and initiation of a new thrust. As soon as new thrust F6 forms in the pre-wedge region, the 50 m displacement position and the failure front both shift to new, but coincident positions (Figs. 13c & 13g). Both the 50 m displacement position and failure front stabilise without significant forward propagation. During this period, the entire system is subject to shortening and thickening in order to establish a critical tapered wedge (Bigi et al., 2010; Wu and McClay, 2011). The strain map (Fig. 13g) shows the formation of a strain localised shear zone which resembles a discrete thrust in natural examples. This stage corresponds to the “after failure and stable sliding phase” of shear tests in granular materials (Lohrmann et al., 2003). During this stage, the strain is primarily released by the new frontal thrust(Dotare et al., 2016).

4) ~2933 m, completion of a cycle (equivalent to ~ 2278 m of shortening). The cycle of *I*6 evolution ends with the development of a new pre-thrust anticline in front of the wedge (Figs. 13d & 13h), which is accompanied by a significant increase of the wedge width and decrease of the taper angle. This phase also marks the start of a new cycle of imbricate block development as a new strain zone forms in the wedge front (Fig. 13h).

4. Discussion

Many previous models have been created and run to test the effects of material rheology on overall thrust belt development, and we have not tried to replicate these approaches. Instead, we have examined the results from a complete model in great detail, which reveals many previously undescribed aspects of thrust wedge growth.

4.1. The episodic growth of the fold-thrust belt

The episodic growth of a thrust belt has been described in many previous studies using a variety of methods including numerical modelling, physical analogue experiments, and field-based structural studies (Mulugeta and Koyi, 1992; Gutscher et al., 1996, 1998; Davis et al., 2006; Del Castello and Cooke, 2007; Ji et al., 2008; Bigi et al., 2010; Cruz et al., 2010; Fitz-Diaz et al., 2014). Although these studies demonstrate the episodic behaviour of thrust wedge growth, a comprehensive quantitative analysis has not yet been reported.

In this study, the taper angle throughout Stage 2 is directly related to the position of the deformation front, which is defined by a zero displacement at surface and migrates as a function of wedge growth (Figs. 2b, c). This definition of taper angle is less subjective compared to the previously used taper angles incorporating the "enveloping wedge slope" (Liu et al., 1992; Gutscher et al., 1996; Schreurs et al., 2006; Wu and McClay, 2011; Sun et al., 2016). The taper angle is then used to determine the critical state of the thrust wedge.

The synthetic diagram of Figure 14 illustrates the clear temporal relationships between the different wedge parameters. The horizontal axis indicates the amount of shortening, a proxy for time, green bars (labelled A3-A6 from left to right) denote phases of wedge accretion, and pink bars (named F4-F6 from left to right) denote periods of new fault initiation. Comparing Figure 14a of the taper angle with Figures 14b and 14c, there are six typical periods of thrust wedge accretion (green bars) which follow gradual evolution of

wedge width, and these periods correlate directly with distinct changes of other variable (i.e., position of 50 m displacement). For example, in the cycle of development of imbricate block *I*4 when the wedge is obtaining a constant apparent critical value ~10° (period between A3 and A4, Fig. 14a), wedge interior, here tracked by the 50 m displacement position, accelerates forward (A3 in Fig. 14c) until a new thrust initiates at the failure front (F4 in Fig. 14c). The wedge then progressively advances until the next wedge accretion phase occurs (F4 to A4 in Fig. 14c). Throughout the process of *I*4 block development, the wedge width gradually increases until a peak value shown by pink bar F4 (Fig. 14b), then followed by a slow decrease before the next wedge accretion phase (A4, Fig. 14b). The peak wedge width coincides with the initiation of a new thrust, occurring at the same time as the failure front rapidly advances forward (F4 in Fig. 14b, c).

The rapid increase in wedge width corresponds to wedge accretion. The evolution of the wedge width in this study is slightly different from that of previous studies, which show that wedge width progressively decreases after thrust formation (Koyi and Vendeville, 2003; Cruz et al., 2010; Wu and McClay, 2011; Ruh et al., 2013; Sun et al., 2016). This is because wedge accretion in previous studies is determined as the formation of the new frontal thrust (Mulugeta and Koyi, 1992; Wu and McClay, 2011), whereas in this study it is determined by incipient folding prior to thrusting. According to our observations (Figs. 3, 7 & 13), this incipient folding develops in advance of establishment of the new thrust fault throughout the wedge growth process. As soon as a new thrust develops at the failure front, by the fault tip breaking through the fold to the surface, the wedge experiences significant shortening. This leads to a slight decrease in wedge width (Fig. 14b) as the entire thrust wedge is subjected to shortening and thickening (Gutscher et al., 1996). At this stage, the wedge is

slowly moving forward as demonstrated by movement of the 50 m displacement position from F4 to A4 in Figure 14c.

Each episode of rapid decrease in taper angle represents a short transition from critical to subcritical taper and coincides with wedge accretion (green bars in Figs. 14a & 14b). The accretion of frontal material builds the wedge forward, thereby increasing wedge width and reducing surface topography (Mulugeta and Koyi, 1992; Gutscher et al., 1996, 1998; Cotton and Koyi, 2000; Koyi and Vendeville, 2003; Bigi et al., 2010; Wu and McClay, 2011; Graveleau et al., 2012). The transition from critical to subcritical taper is rapid with respect to the time period when the thrust wedge is attaining its critical taper (A3 to A4 in Fig 14a). Similar results have been observed in physical analogues (Gutscher et al., 1996; Wang and Davis, 1996; Dotare et al., 2016; Schreurs et al., 2016; Sun et al., 2016) and numerical experiments (Buiter et al., 2006; Cruz et al., 2010; Buiter et al., 2016) but the interaction between different wedge parameters during this transitional period had not previously been analysed in detail.

The rapid propagation of the failure front, as a new fault initiates (pink bars in Fig. 14c), lags behind the propagation of the 50 m displacement position (green bars in Fig. 14c). But the failure front completes its rapid propagation within one shortening period, effectively "jumping" to a new position with the formation of a discrete fault, whereas the 50 m displacement position propagates over several shortening periods (Fig. 14c). Both the failure front and 50 m displacement position complete their advancement phases simultaneously, despite differing in initiation time (Fig. 14d). A total of 6 short episodes are observed when the thrust wedge is transferring from critical to subcritical taper as a result of wedge accretion (represented by green bars), dividing the overall process of wedge building into 7

periods. Therefore, a typical cycle of creating a thrust wedge (one period) involves growth through a combination of rapid advancement of the thrust belt and slow building of the wedge (see examples of *I*6 in Figs. 13& 14).

In the case of high basal friction (80%-90% of the internal friction), cyclic behaviour has been observed in analogue models, alternating between frontal accretion of imbricate thrust slices and basal accretion of underthrusting of long, undeformed sheets (Gutscher et al., 1996). In this study, where the basal friction (μ_b=0.3) is half of the internal friction (μ=0.6), i.e., relatively low, the episodic and cyclic growth of the thrust wedge is still observed, but dominantly through frontal accretion. Therefore, the ratio of basal friction to internal friction is not a precondition for cyclical growth of a fold-thrust belt as long as the basal detachment is not stronger than the wedge material for the existence of a critical Coulomb Wedge (Dahlen, 1984; Bilotti and Shaw, 2005; Fagereng, 2011). But the ratio of basal friction over internal friction exerts a first order control on the growth mechanism of thrust wedge i.e., frontal accretion, basal accretion or mixture of both. As such, the resultant structures in an accretionary prism appear to be indicative of the basal strength; development of the imbricate thrust slices suggest low basal friction (i.e., 50% of the internal friction) while the under-thrusting implies high basal friction (i.e., 80%-90% of the internal friction).

To reveal in detail the internal deformation of the pre-wedge region and the forward propagation of the thrust wedge, we tracked the 0-50 m displacement contours and analysed the strain distribution in our models (Figs. 7, 13, 14). Our results show that there is clear, although minor, deformation (0-10 m displacement) in front of the thrust wedge, which distinguishes the failure front from the displacement front throughout fold-thrust

belt development (Fig. 13). This indicates that frontal accretion starts with small scale displacement of material and minor strain accumulation characterised by pre-thrust folding, which is followed by subsequent thrusting after additional convergence. This spatial and temporal relationship has been recognized from natural examples in the form of proto-thrust zones (Wang et al., 1994; Moore et al., 2001; Adam et al., 2004; Gulick et al., 2004; Lin et al., 2009; Ghisetti et al., 2016) and some modelling/experimental studies (Yamada et al., 2006; Dotare et al., 2016), however, through examining the process of initiation of a thrust fault, we have been able to quantify and determine the timing and significance of this small amount of deformation (Fig. 13). The integrated analysis (Fig. 14) suggests that the evolution of minor deformation in the pre-wedge region is episodic, with each phase resulting in the establishment of a new imbricate block (Fig. 13) as a new cycle of wedge building starts. Without this minor deformation, the thrust belt is unable to propagate forwards.

4.2. The thrust wedge development process

Figure 15 illustrates the sequence of events during a typical cycle of fold-thrust belt growth, the pink and green background colour corresponds to the pink and green bars in Figure 14 and the size of the black arrows represents the relative displacements. In order to achieve a critical taper, the wedge has to deform internally which effectively results in movement along a pre-existing thrust (Fig. 15a) as the deformation front propagates forward. As soon as wedge accretion occurs, the material within the wedge advances rapidly toward the locus of new folding at the deformation front (beyond the region of thrust faulting), leading to a significant increase in wedge width (Fig. 15b). Wedge material rapidly moves towards the newly formed fold where the strain is localised (Fig. 15c). As additional

strain builds up in the folding area, a new thrust starts to form and propagates upwards to break the existing fold with its fault tip reaching the wedge surface (Fig. 15d). It is worth noting that, in the FE model, thrusts are represented and modelled as strain localised shear zones which differ from discrete thrusts that break through folds in natural examples. Major displacement (see Figs. 13b & 13c) then takes places within the new thrust zone and the wedge interior deforms to re-establish its critical taper (Fig. 15e), resulting in decreased wedge width (see pink bars in Fig. 14). Similar to the phase in Figure 15a, pre-formed thrusts reactivate so as to build up the taper angle to critical while the internal movement of the wedge slows, marking the start of another cycle (Fig. 15e).

5. Conclusions

By monitoring multiple wedge parameters, this study provides new insights into deformation during cycles of thrust accretion as a fold-thrust belt or wedge develops. Integration of these parameters into a synthetic diagram (Fig. 14) and comparison of the rates of change of these parameters show how they interact and how the wedge uplifts and propagates in response to continuous shortening and frontal accretion. The results clearly indicate that the development of a fold-thrust belt occurs through growth stages that repeat cyclically and episodically as the system undergoes continuous shortening. The key findings are:

1) A fold-thrust system can be broken down into three primary deformation components – the thrust wedge, pre-wedge and undeformed region (Fig. 4), which are characterised by distinct deformation processes and phases of deformation and can be recognised throughout the wedge development process.

2) In the early stage (Stage 1 in this study), a composite thrust wedge is built adjacent to the mobile wall and this builds a critical taper. The wedge then propagates forward by the sequential development of new imbricate thrust blocks (*I*4, *I*5 & *I*6).

3) As soon as thrust accretion occurs, the wedge width increases significantly reducing the taper angle below critical whilst the wedge interior (tracked by the 50 m displacement position) rapidly propagates forward (green bars in Fig. 14).

4) During attainment of a critical taper, the wedge experiences significant shortening after a new thrust initiates, leading to a decrease in wedge width (pinks bars on Fig. 14). Successive widening of the wedge and subsequent shortening and thrusting maintain a reasonably constant taper angle.

5) The rapid propagation of the failure front as a new fault initiates (pink bars) lags behind that of the 50 m displacement position (green bars, Fig. 14). Both parameters complete their advancement phases simultaneously.

6) The fold-thrust belt evolves cyclically, through a combination of rapid advancement of the fold-thrust belt and gradual, slow building of the wedge (example *I*4 in Figs. 13 & 14).

7) Minor deformation at the front of the thrust wedge is quantified. The results clearly indicate minor deformation (0-10 m displacement) in front of the thrust wedge. This zone of deformation separates the failure front from the displacement front and without this minor deformation, the wedge is unable to move forward.

Acknowledgements

We acknowledge funding to X. Yang from the Natural Environment Research Council (NERC) Centre for Doctoral Training (CDT) in Oil and Gas and the University of Southampton.

We thank S. Ellis for sharing her model and her suggestions to modify the model settings, and we are grateful to S. Buiter and J. Suppe for helpful discussions. We thank the two reviewers, J. Adam and S. Ellis, for extremely helpful and constructive reviews that improved the manuscript.

References

Adam, J., Klaeschen, D., Kukowski, N., Flueh, E., 2004. Upward delamination of Cascadia Basin sediment infill with landward frontal accretion thrusting caused by rapid glacial age material flux. Tectonics 23, TC3009.

Adam, J., Klinkmüller, M., Schreurs, G., Wieneke, B., 2013. Quantitative 3D strain analysis in analogue experiments simulating tectonic deformation: Integration of X-ray computed tomography and digital volume correlation techniques. Journal of Structural Geology 55, 127-149.

Adam, J., Urai, J.L., Wieneke, B., Oncken, O., Pfeiffer, K., Kukowski, N., Lohrmann, J., Hoth, S., van der Zee, W., Schmatz, J., 2005. Shear localisation and strain distribution during tectonic faulting - new insights from granular-flow experiments and high-resolution optical image correlation techniques. Journal of Structural Geology 27, 283-301.

Barnes, P.M., Lamarche, G., Bialas, J., Henrys, S., Pecher, I., Netzeband, G.L., Greinert, J., Mountjoy, J.J., Pedley, K., Crutchley, G., 2010. Tectonic and geological framework for gas hydrates and cold seeps on the Hikurangi subduction margin, New Zealand. Marine Geology 272, 26-48.

Beaumont, C., Fullsack, P., Hamilton, J., 1992. Erosional control of active compressional orogens, in: McClay, K.R. (Ed.), Thrust Tectonics. Chapman and Hall, London, pp. 1-18.

Bigi, S., Di Paolo, L., Vadacca, L., Gambardella, G., 2010. Load and unload as interference factors on cyclical behavior and kinematics of Coulomb wedges: Insights from sandbox experiments. Journal of Structural Geology 32, 28-44.

Bilotti, F., Shaw, J.H., 2005. Deep-water Niger Delta fold and thrust belt modeled as a critical-taper wedge: The influence of elevated basal fluid pressure on structural styles. AAPG Bulletin 89, 1475-1491.

Bose, S., Mandal, N., Mukhopadhyaly, D.K., Mishra, P., 2009. An unstable kinematic state of the Himalayan tectonic wedge: Evidence from experimental thrust-spacing patterns. Journal of Structural Geology 31, 83-91.

Braathen, A., Bergh, S.G., Maher, J., H. D., 1999. Application of a critical wedge taper model to the Tertiary transpressional fold-thrust belt on Spitsbergen, Svalbard. Geologcial Society of America Bulletin 111, 1468-1685.

Buiter, S.J., Schreurs, G., Albertz, M., Gerya, T.V., Kaus, B., Landry, W., le Pourhiet, L., Mishin, Y., Egholm, D.L., Cooke, M., 2016. Benchmarking numerical models of brittle thrust wedges. Journal of Structural Geology 92, 140-177.

Buiter, S.J.H., 2012. A review of brittle compressional wedge models. Tectonophysics 530, 1-17.

Buiter, S.J.H., Babeyko, A.Y., Ellis, S., Gerya, T.V., Kaus, B.J.P., Kellner, A., Schreurs, G., Yamada, Y., 2006. The numerical sandbox: Comparison of model results for a shortening and

an extension experiment, in: Buiter, S.J.H., Schreurs, G. (Eds.), Analogue and Numerical Modelling of Crustal-Scale Processes, pp. 29-64.
Burbidge, D.R., Braun, J., 2002. Numerical models of the evolution of accretionary wedges and fold-and-thrust belts using the distinct-element method. Geophysical Journal International 148, 542-561.
Byrne, T., Fisher, D., 1987. Episodic growth of the Kodiak convergent margin. Nature 325, 338-341.
Chapple, W.M., 1978. Mechanics of thin-skinned fold-and-thrust belts. Geological Society of America Bulletin 89, 1189-1198.
Cotton, J.T., Koyi, H.A., 2000. Modeling of thrust fronts above ductile and frictional detachments: Application to structures in the Salt Range and Potwar Plateau, Pakistan. Geological Society of America Bulletin 112, 351-363.
Cruz, L., Malinski, J., Wilson, A., Take, W.A., Hilley, G., 2010. Erosional control of the kinematics and geometry of fold-and-thrust belts imaged in a physical and numerical sandbox. Journal of Geophysical Research-Solid Earth 115, B09404.
Dahlen, F.A., 1984. Noncohesive critical coulomb wedges-an exact solution. Journal of Geophysical Research 89, 125-133.
Dahlen, F.A., 1990. Critical taper model of fold-and-thrust belts and accretionary wedges. Annual Review of Earth and Planetary Sciences 18, 55-99.
Dahlen, F.A., Suppe, J., Davis, D., 1984. Mechanics of fold-and-thrust belts and accretionary wedges-cohesive coulomb theory. Journal of Geophysical Research 89, 87-101.
Davis, D., Suppe, J., Dahlen, F.A., 1983. Mechanics of fold-and-thrust belts and accretionary wedges. Journal of Geophysical Research 88, 1153-1172.
Davis, E.E., Becker, K., Wang, K.L., Obara, K., Ito, Y., Kinoshita, M., 2006. A discrete episode of seismic and aseismic deformation of the Nankai trough subduction zone accretionary prism and incoming Philippine Sea plate. Earth and Planetary Science Letters 242, 73-84.
Del Castello, M., Cooke, M.L., 2007. Underthrusting-accretion cycle: Work budget as revealed by the boundary element method. Journal of Geophysical Research 112, B12404.
Dotare, T., Yamada, Y., Adam, J., Hori, T., Sakaguchi, H., 2016. Initiation of a thrust fault revealed by analog experiments. Tectonophysics 684, 148-156.
Ellis, S., Schreurs, G., Panien, M., 2004. Comparisons between analogue and numerical models of thrust wedge development. Journal of Structural Geology 26, 1659-1675.
Fagereng, A., 2011. Wedge geometry, mechanical strength, and interseismic coupling of the Hukurangi subduction thrust, New Zealand. Tectonophysics 507, 26-30.
Fillon, C., Huismans, R., van der Beek, P., 2012. Syntectonic sedimentation effects on the growth of fold and thrust belts. Geology 41, 83-86.
Fitz-Diaz, E., Hudleston, P., Tolson, G., van der Pluijm, B., 2014. Progressive, episodic deformation in the Mexican Fold–Thrust Belt (central Mexico): evidence from isotopic dating of folds and faults. International Geology Review 56, 734-755.
Ghisetti, F.C., Barnes, P.M., Ellis, S., Plaza‐Faverola, A.A., Barker, D.H., 2016. The last 2 Myr of accretionary wedge construction in the central Hikurangi margin (North Island, New Zealand): Insights from structural modeling. Geochemistry, Geophysics, Geosystems 17, 2661-2686.
Graveleau, F., Malavieille, J., Dominguez, S., 2012. Experimental modelling of orogenic wedges: A review. Tectonophysics 538, 1-66.
Gulick, S.P.S., Bangs, N.L.B., Shipley, T.H., Nakamura, Y., Moore, G., Kuramoto, S., 2004. Three-dimensional architecture of the Nankai accretionary prism's imbricate thrust zone off

Cape Muroto, Japan: Prism reconstruction via en echelon thrust propagation. Journal of Geophysical Research 109, B02105.
Gutscher, M.A., Kukowski, N., Malavieille, J., Lallemand, S., 1996. Cyclical behavior of thrust wedges: Insights from high basal friction sandbox experiments. Geology 24, 135-138.
Gutscher, M.A., Kukowski, N., Malavieille, J., Lallemand, S., 1998. Episodic imbricate thrusting and underthrusting: Analog experiments and mechanical analysis applied to the Alaskan accretionary wedge. Journal of Geophysical Research 103, 10161-10176.
Hoth, S., Adam, J., Kukowski, N., Oncken, O., 2006. Influence of erosion on the kinematics of bivergent orogens: Results from scaled sandbox simulations. Tectonics, Climate, and Landscape Evolution 398, 201-225.
Ji, J., Luo, P., White, P., Jiang, H., Gao, L., Ding, Z., 2008. Episodic uplift of the Tianshan Mountains since the late Oligocene constrained by magnetostratigraphy of the Jingou River section, in the southern margin of the Junggar Basin, China. Journal of Geophysical Research-Solid Earth 113.
Karig, D., Lundberg, N., 1990. Deformation bands from the toe of the Nankai accretionary prism. Journal of Geophysical Research 95, 9099-9109.
Koyi, H., 1995. Mode of internal deformation in sand wedges. Journal of Structural Geology 17, 293-&.
Koyi, H.A., Vendeville, B.C., 2003. The effect of decollement dip on geometry and kinematics of model accretionary wedges. Journal of Structural Geology 25, 1445-1450.
Ku, C.-Y., Hsu, S.-K., 2009. Crustal structure and deformation at the northern Manila Trench between Taiwan and Luzon islands. Tectonophysics 466, 229-240.
Lallemand, S., Le Pichon, X., 1987. Coulomb wedge model applied to the subduction of seamounts in the Japan Trench. Geology 15, 1065-1069.
Lease, R.O., Burbank, D.W., Hough, B., Wang, Z., Yuan, D., 2012. Pulsed Miocene range growth in northeastern Tibet: Insights from Xunhua Basin magnetostratigraphy and provenance. Geological Society of America Bulletin 124, 657-677.
Lin, A.T., Yao, B., Hsu, S.-K., Liu, C.-S., Huang, C.-Y., 2009. Tectonic features of the incipient arc-continent collision zone of Taiwan: implications for seismicity. Tectonophysics 479, 28-42.
Liu, H.Q., McClay, K.R., Powell, D., 1992. Physical models of thrust wedges, in: McClay, K.R. (Ed.), Thrust Tectonics. Chapman and Hall, London, pp. 71-81.
Lohrmann, J., Kukowski, N., Adam, J., Oncken, O., 2003. The impact of analogue material properties on the geometry, kinematics, and dynamics of convergent sand wedges. Journal of Structural Geology 25, 1691-1711.
MacKay, M.E., 1995. Structural variation and landward vergence at the toe of the Oregon accretionary prism. Tectonics 14, 1309-1320.
Marques, F.O., Cobbold, P.R., 2002. Topography as a major factor in the development of arcuate thrust belts: insights from sandbox experiments. Tectonophysics 348, 247-268.
Marques, F.O., Cobbold, P.R., 2006. Effects of topography on the curvature of fold-and-thrust belts during shortening of a 2-layer model of continental lithosphere. Tectonophysics 415, 65-80.
Masaferro, J.L., Poblet, J., Bulnes, M., Eberli, G.P., Dixon, T.H., McClay, K., 1999. Palaeogene-Neogene/present day(?) growth folding in the Bahamian foreland of the Cuban fold and thrust belt. Journal of the Geological Society 156, 617-631.
McClay, K.R., Whitehouse, P.S., Dooley, T., Richards, A., 2004. 3D evolution of fold and thrust belts formed by oblique convergence. Marine and Petroleum Geology 21, 857-877.

Moore, G.F., Taira, A., Klaus, A., Becker, L., Boeckel, B., Cragg, B.A., Dean, A., Fergusson, C.L., Henry, P., Hirano, S., 2001. New insights into deformation and fluid flow processes in the Nankai Trough accretionary prism: Results of Ocean Drilling Program Leg 190. Geochemistry, Geophysics, Geosystems 2, 2001GC000166.
Mouthereau, F., Lacombe, O., Meyer, B., 2006. The Zagros folded belt(Fars, Iran): constraints from topography and critical wedge modelling. Geophysical Journal International 165, 336-356.
Mulugeta, G., 1988. Modeling the geometry of coulomb thrust wedges. Journal of Structural Geology 10, 847-859.
Mulugeta, G., Koyi, H., 1992. Episodic accretion and strain partitioning in a model sand wedge. Tectonophysics 202, 319-333.
Panien, M., Schreurs, G., Pfiffner, A., 2006. Mechanical behaviour of granular materials used in analogue modelling: insights from grain characterisation, ring-shear tests and analogue experiments. Journal of Structural Geology 28, 1710-1724.
Platt, J.P., 1986. Dynamics of orogenic wedges and the uplift of high pressure metamorphic rocks. Geological Society of America Bulletin 97, 1037-1053.
Ruh, J.B., Gerya, T., Burg, J.P., 2013. High‐resolution 3D numerical modeling of thrust wedges: Influence of décollement strength on transfer zones. Geochemistry, Geophysics, Geosystems 14, 1131-1155.
Ruh, J.B., Kaus, B.J.P., Burg, J.-P., 2012. Numerical investigation of deformation mechanics in fold-and-thrust belts: Influence of rheology of single and multiple decollements. Tectonics 31, TC3005.
Schreurs, G., Buiter, S.J., Boutelier, J., Burberry, C., Callot, J.-P., Cavozzi, C., Cerca, M., Chen, J.-H., Cristallini, E., Cruden, A.R., 2016. Benchmarking analogue models of brittle thrust wedges. Journal of Structural Geology 92, 116-139.
Schreurs, G., Buiter, S.J.H., Boutelier, D., Corti, G., Costa, E., Cruden, A.R., Daniel, J.-M., Hoth, S., Koyi, H.A., Kukowski, N., Lohrmann, J., Ravaglia, A., Schlische, R.W., Withjack, M.O., Yamada, Y., Cavozzi, C., Del Ventisette, C., Brady, J.A.E., Hoffmann-Rothe, A., Mengus, J.-M., Montanari, D., Nilforoushan, F., 2006. Analogue benchmarks of shortening and extension experiments, in: Buiter, S.J.H., Schreurs, G. (Eds.), Analogue and Numerical Modelling of Crustal-Scale Processes, pp. 1-27.
Selzer, C., Buiter, S.J.H., Pfiffner, O.A., 2007. Sensitivity of shear zones in orogenic wedges to surface processes and strain softening. Tectonophysics 437, 51-70.
Selzer, C., Buiter, S.J.H., Pfiffner, O.A., 2008. Numerical modeling of frontal and basal accretion at collisional margins. Tectonics 27, TC3001.
Sherkati, S., Letouzey, J., de Lamotte, D.F., 2006. Central Zagros fold-thrust belt (Iran): New insights from seismic data, field observation, and sandbox modeling. Tectonics 25, TC4007.
Simpson, G.D.H., 2006. Modelling interactions between fold-thrust belt deformation, foreland flexure and surface mass transport. Basin Research 18, 125-143.
Simpson, G.D.H., 2009. Mechanical modelling of folding versus faulting in brittle-ductile wedges. Journal of Structural Geology 31, 369-381.
Simpson, G.D.H., 2010a. Formation of accretionary prisms influenced by sediment subduction and supplied by sediments from adjacent continents. Geology 38, 131-134.
Simpson, G.D.H., 2010b. Influence of the mechanical behaviour of brittle-ductile fold-thrust belts on the development of foreland basins. Basin Research 22, 139-156.
Smit, J.H.W., Brun, J.P., Sokoutis, D., 2003. Deformation of brittle-ductile thrust wedges in experiments and nature. Journal of Geophysical Research 108, 2480.

Stockmal, G.S., Beaumont, C., Nguyen, M., Lee, B.,, 2007. Mechanics of thin-skinned fold and-thrust belts: insights from numerical models. Geological Society of America Bulletin Whence the Mountains? Inquiries into the Evolution of Orogenic Systems: A Volume in Honor of Raymond A. Price, 63-98.
Storti, F., McClay, K., 1995. Influence of syntectonic sedimentation on thrust wedges in analog models. Geology 23, 999-1002.
Sun, C., Jia, D., Yin, H., Chen, Z., Li, Z., Shen, L., Wei, D., Li, Y., Yan, B., Wang, M., 2016. Sandbox modeling of evolving thrust wedges with different preexisting topographic relief: Implications for the Longmen Shan thrust belt, eastern Tibet. Journal of Geophysical Research: Solid Earth 121, 4591-4614.
Suppe, J., 2007. Absolute fault and crustal strength from wedge tapers. Geology 35, 1127-1130.
Tsuji, T., Matsuoka, T., Yamada, Y., Nakamura, Y., Ashi, J., Tokuyama, H., Kuramoto, S.i., Bangs, N.L., 2005. Initiation of plate boundary slip in the Nankai Trough off the Muroto peninsula, southwest Japan. Geophysical Research Letters 32, L12306.
Tuitt, A., King, R., Hergert, T., Tingay, M., Hillis, R., 2012. Modelling of sediment wedge movement along low-angle detachments using ABAQUS™. Geological Society, London, Special Publications 367, 171-183.
von Hagke, C., Oncken, O., Evseev, S., 2014. Critical taper analysis reveals lithological control of variations in detachment strength: An analysis of the Alpine basal detachment (Swiss Alps). Geochemistry Geophysics Geosystems 15, 176-191.
Wang, C.y., Hwang, W.t., Cochrane, G.R., 1994. Tectonic dewatering and mechanics of protothrust zones: example from the Cascadia accretionary margin. Journal of Geophysical Research 99, 20043-20050.
Wang, W.H., Davis, D.M., 1996. Sandbox model simulation of forearc evolution and noncritical wedges. Journal of Geophysical Research 101, 11329-11339.
Willett, S.D., 1992. Dynamic and kinematic growth and change of a coulomb wedge.
Woodward, N.B., 1987. Geological applicability of critical-wedge thrust-belt models. Geological Society of America Bulletin 99, 827-832.
Wu, J.E., McClay, K.R., 2011. Two-dimensional analog modelling of fold and thrust belts: dynamic interactions with syncontractional sedimentation and erosion AAPG Bulletin 94, 301-333.
Yamada, Y., Baba, K., Matsuoka, T., 2006. Analogue and numerical modelling of accretionary prisms with a decollement in sediments, in: Buiter, S.J.H., Schreurs, G. (Eds.), Analogue and Numerical Modelling of Crustal-Scale Processes, pp. 169-183.
Zhao, W.L., Davis, D.M., Dahlen, F.A., Suppe, J., 1986. Orign of convex accretionary wedges-evidence from Barbados. Journal of Geophysical Research-Solid Earth and Planets 91, 246-258.
Zhou, J., Zhang, B., Xu, Q., 2016. Effects of lateral friction on the structural evolution of fold-and-thrust belts: Insights from sandbox experiments with implications for the origin of landward-vergent thrust wedges in Cascadia. Geological Society of America Bulletin 128, 669-683.

Figure Captions

Fig. 1. Conceptual cartoon illustrating the difference between the theoretical Coulomb wedge model and a real world example. (a) Simple Coulomb Wedge Model (CWM), which retains a constant shape as it moves, α and β are topographic slope and detachment dip, respectively, ψ_b and ψ_0 are the angles between the maximum principal compressive stress σ_1 and base and top of the wedge; (b) Model with sediment layer in front of wedge; (c) Simple Coulomb Model without advance of wedge front; (d) Accretion by imbrication on large discrete thrusts that will change the wedge shape and taper with time.

Fig. 2. Setup of the thrust wedge experiments and illustration of wedge parameters at different shortening periods. (a) Setup of thrust wedge model, a horizontal sand layer with width of 10000 m and thickness of 600 m is shortened by a mobile wall running from left to right, while the base and right wall remain fixed. (b) Schematic illustration of the approach followed for measurements of wedge parameters. *a* = displacement front, defined as position of 0 m displacement along the detachment, *b* = 50 m displacement position along the detachment, *c* = failure front where the frontal thrust roots into the detachment, *d* = deformation front (in this case, the frontal thrust tip), *e* = inboard corner of the wedge, *f* = overall taper angle determined by the slope of straight line from *e* to *d*. (c) Schematic showing the measurements of additional wedge parameters. As further shortening is added, a new fold is formed in front of the existing thrust. A new thrust is about to initiate to break the new fold with its fault tip reaching the wedge surface at the deformation front *d*. *g* = surface slope determined as the best fitting line enveloping the thrust

wedge (Schreurs et al., 2006), h = height of the thrust wedge, w= wedge width determined by the distance from deformation front *d* to the moving left hand wall.

Fig. 3. Sequential development of the thrust belt model. ΔX indicates the amount of shortening. The enlarged region shows the cell along the shear zone is significantly deformed, elongated and tilted towards the foreland.

Fig. 4. Thrust model after 3268 m of shortening, showing the principal structural elements discussed in the text. *I*1 to *I*6 are the major imbricate fault blocks. F1-F6 are the major thrust faults. Dotted thin red lines in fault blocks *I*4 and *I*6 are significant short-cut faults. Blue line is an originally continuous stratigraphic marker. The thrust system can be divided into a thrust wedge, pre-wedge, and undeformed region.

Fig. 5. Plot of surface slope (green) and taper angle (purple) against shortening. Stage 1 is the initial wedge building phase which is largely controlled by boundary conditions and velocity discontinuity, while Stage 2 (beyond 700 m shortening) is a steady state phase of thrust wedge development which is thought to be highly relevant to natural thrust systems.

Fig. 6. (a) Wedge width and height against shortening with an inserted figure enlarging the initial phase of wedge width growth over 0-700 m of shortening. With Stage 2, 4 wedge accretions can be recognised where the wedge width rapidly increases. b) Growth rate of wedge height versus shortening. The growth rate at Stage 1 is typically higher than that in Stage 2.

Fig. 7. A model example of a fold-thrust belt with total shortening of 2300 m. (a),(b) and (c) show the fully scaled distribution of the total, horizontal and vertical displacement in the wedge; (d),(f) and (e) present the total, horizontal and vertical displacement

scaled to 0-50 m in the wedge front showing the displacement front and the 0-50 m displacement contours with focus on small scale deformation. The failure front is where the frontal thrust roots into the detachment.

Fig. 8. Evolution of horizontal displacement (X coordinate value) front vs. shortening. (a) Position of displacement front against shortening. (b) Rate of propagation of the displacement front against shortening (same method as calculated growth rate of wedge height, Fig. 7b), black arrows indicate the low propagation rate phases within each cyclic period.

Fig. 9. Position of 50 m displacement (X coordinate value) vs. shortening. (a) Plot of 50 m displacement position against shortening with inset enlarging the initial 0-700m of shortening. (b) Propagation rate of the 50 m displacement position against shortening.

Fig.10. (a) Position of failure front (X coordinate value) against shortening, inset enlarging the initial 0-800 m of shortening. (b) Propagation rate of the failure front against shortening.

Fig. 11. Evolution of associated parameters with thrust wedge advancement vs. shortening. (a) Position of displacement front, 50 m displacement position and failure front against shortening. (b) Propagation rate of displacement front, 50 m displacement and failure front against shortening.

Fig. 12. A synthetic diagram showing the evolution of shortening vs. the displacement front, 50 m displacement and failure front.

Fig. 13. Model results of horizontal displacement and principal strain showing cyclic

evolution of imbricate thrust block *I*6 through a cycle of thrust wedge development. ΔX indicates the amount of shortening. (a) Wedge accretion after 2278 m of shortening. (b) Diffused deformation over the incipient folding. (c) Strain localisation and initiation of new thrust at the failure front after 2766m of shortening. (d) The completion of a cycle. (e) – (h) show the corresponding strain distribution at the same 4 stages as (a)-(d).

Fig. 14. Time relationship of different wedge parameters. Horizontal axis for plots is shortening, a proxy for time. Green bars (named A3-A6 from left to right) denote wedge accretion phases in which the taper angle drops immediately after obtaining a critical taper; pink bars (named F4-F6 from left to right) donate periods of new fault initiation. *I*4, *I*5 and *I*6 represent the periods of development of imbricate blocks between wedge accretion phases. (a) Plot of taper angle against the amount of shortening. (b) Plot of wedge width and height against the amount of shortening. (c) Plot of the displacement front, 50 m displacement and failure front versus the amount of shortening. Both green and red bands show the correlation between different deformation parameters throughout the process.

Fig. 15. Schematic sections showing how the observed cyclic behaviour in the numerical model relates to the cyclicity of tectonic processes in the thrust wedge. Pink (new fault initiation) and green background (wedge accretion) corresponds to the pink and green bars in Figure 14. The size of black arrow represents the scale of displacement in the process of wedge growth.

Tables

Table 1. Material properties used in the wedge models

Material	D (kg m^{-3})	φ_{peak} (°)	φ_{stable} (°)	E (MPa)	ν	G ($m*s^{-2}$)	ψ (°)	C （Pa）	η (Pa s)	μ_b	μ_s
Wedge	1560	36	31	5e10	0.25	10	0.1	10	5e4	0.3	0.075
Basement and two walls	2800			5e12	0.25		0.1				

D=Density, φ_{peak}=Angle of internal friction at peak strength, φ_{stable}=Angle of internal friction at stable strength, E=Young's modulus, ν=Poisson's ratio, G=Gravitational acceleration, ψ=Angle of dilation, C=Cohesion, η=Viscosity, μ_b=coefficient of basal friction, μ_s=coefficient of side friction.

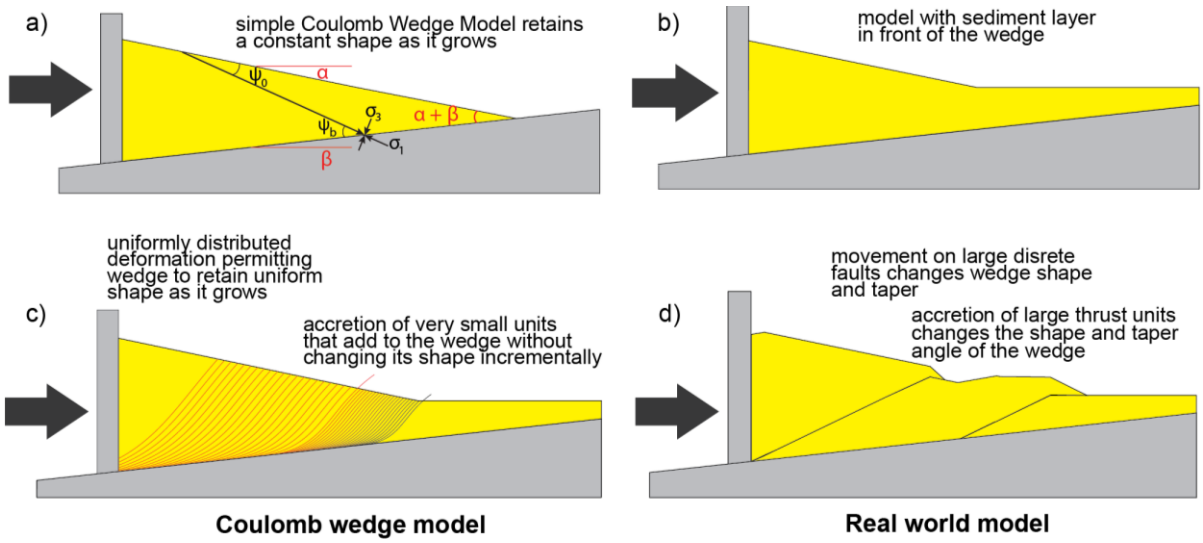
a)
simple Coulomb Wedge Model retains
a constant shape as it grows
ψo
α
σ3
α + β
ψb
σ1
β
b)
model with sediment layer
in front of the wedge
c)
uniformly distributed
deformation permitting
wedge to retain uniform
shape as it grows
accretion of very small units
that add to the wedge without
changing its shape incrementally
d)
movement on large disrete
faults changes wedge shape
and taper
accretion of large thrust units
changes the shape and taper
angle of the wedge
Coulomb wedge model
Real world model

Fig 1.

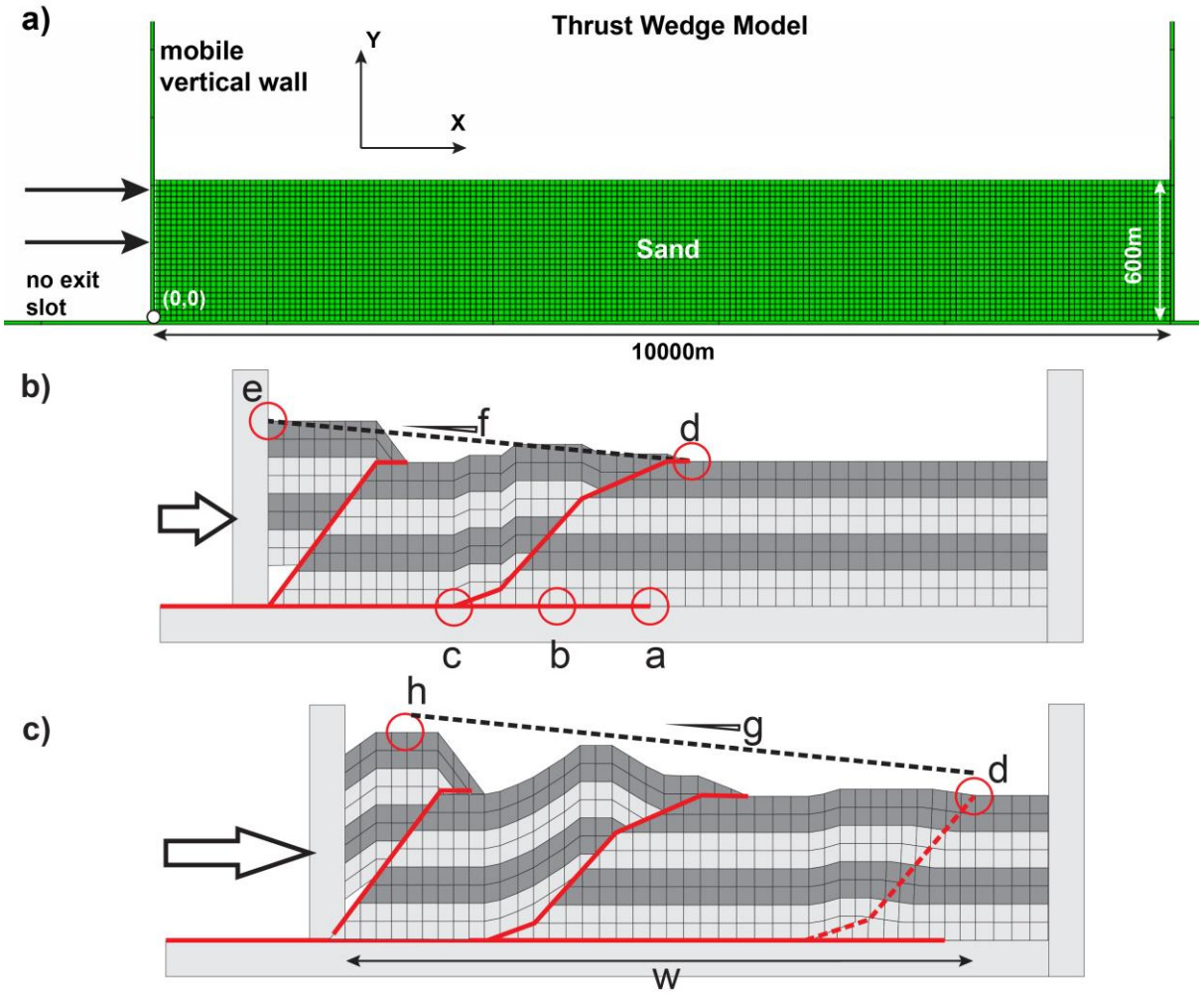
a)
Thrust Wedge Model
mobile
vertical wall
Y
X
Sand
600m
no exit
slot
(0,0)
10000m
b)
e
f
d
c
b
a
c)
h
g
d
w

Fig. 2.

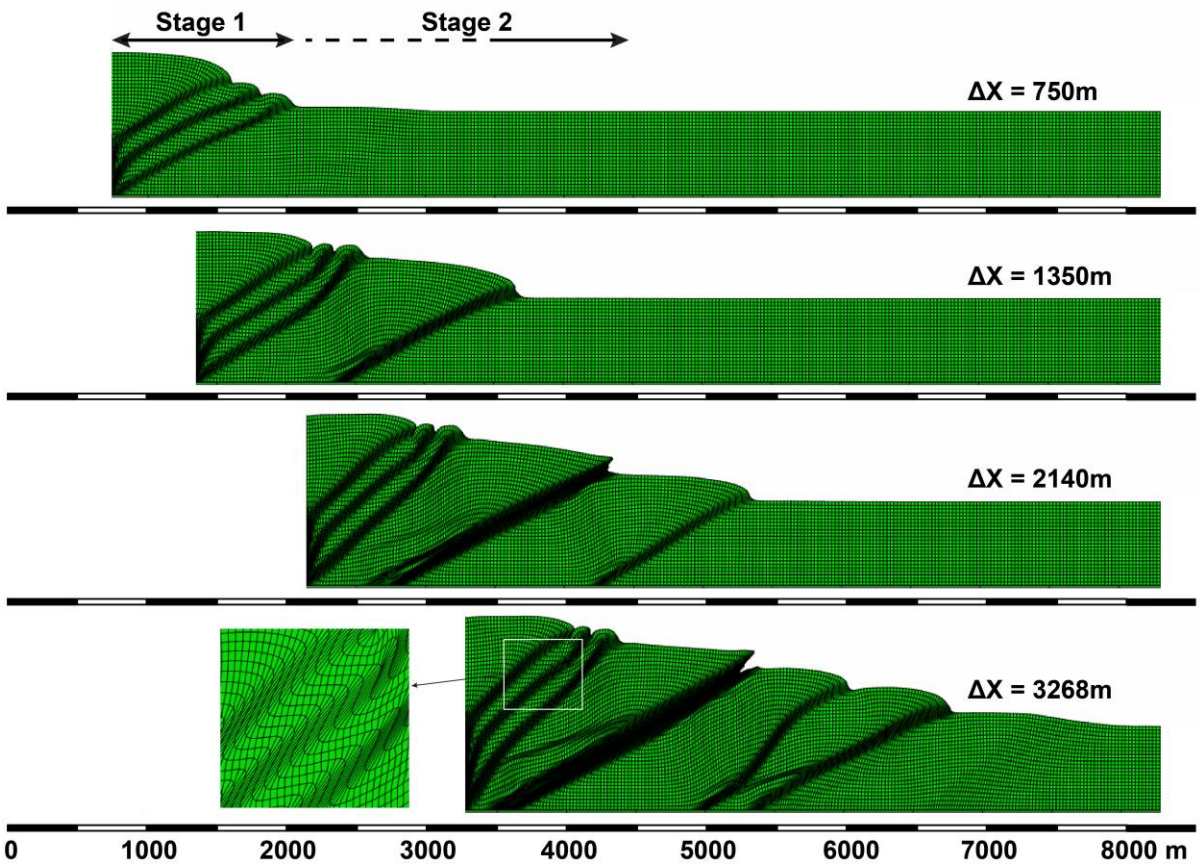
Stage 1
Stage 2
ΔX = 750m
ΔX = 1350m
ΔX = 2140m
ΔX = 3268m
0
1000
2000
3000
4000
5000
6000
7000
8000 m

Fig. 3.

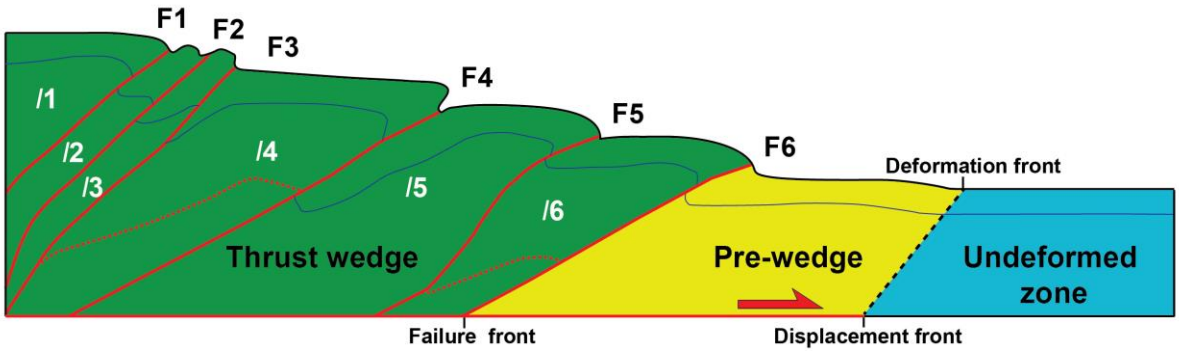
F1
F2
F3
F4
F5
F6
/1
/2
/3
/4
/5
/6
Deformation front
Thrust wedge
Pre-wedge
Undeformed zone
Failure front
Displacement front

Fig. 4.

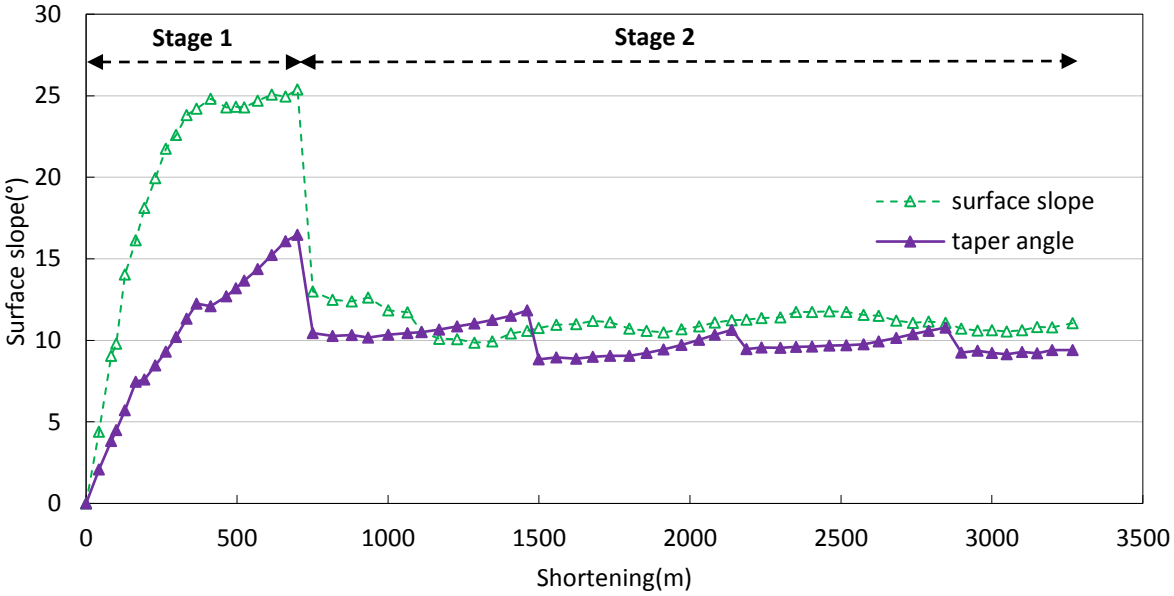
Stage 1
Stage 2
surface slope
taper angle
Surface slope(°)
Shortening(m)
0
5
10
15
20
25
30
0
500
1000
1500
2000
2500
3000
3500

Fig. 5.

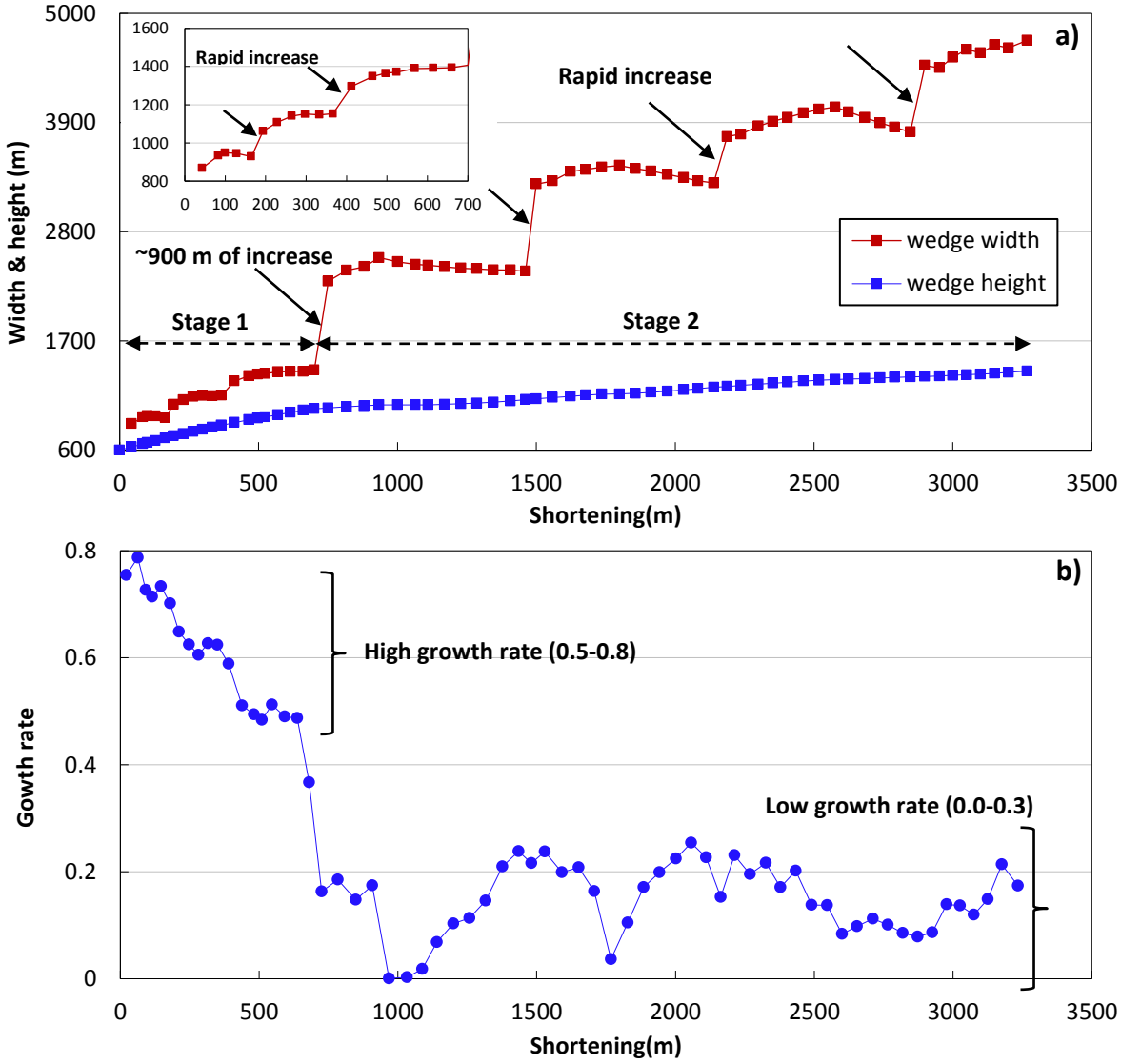
a)
Width & height (m)
5000
3900
2800
1700
600
0
500
1000
1500
2000
2500
3000
3500
Shortening(m)
Rapid increase
~900 m of increase
Stage 1
Stage 2
wedge width
wedge height
1600
1400
1200
1000
800
0
100
200
300
400
500
600
700
b)
Gowth rate
0.8
0.6
0.4
0.2
0
High growth rate (0.5-0.8)
Low growth rate (0.0-0.3)

Fig. 6.

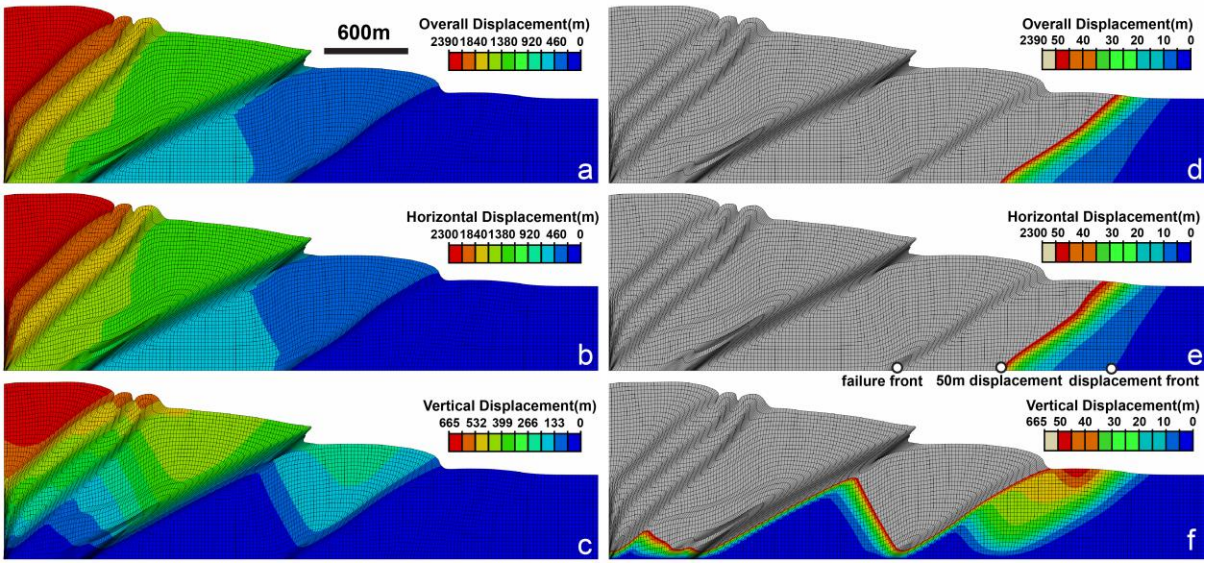
600m
Overall Displacement(m)
2390 1840 1380 920 460 0
a
Horizontal Displacement(m)
2300 1840 1380 920 460 0
b
Vertical Displacement(m)
665 532 399 266 133 0
c
Overall Displacement(m)
2390 50 40 30 20 10 0
d
Horizontal Displacement(m)
2300 50 40 30 20 10 0
e
failure front
50m displacement
displacement front
Vertical Displacement(m)
665 50 40 30 20 10 0
f

Fig. 7.

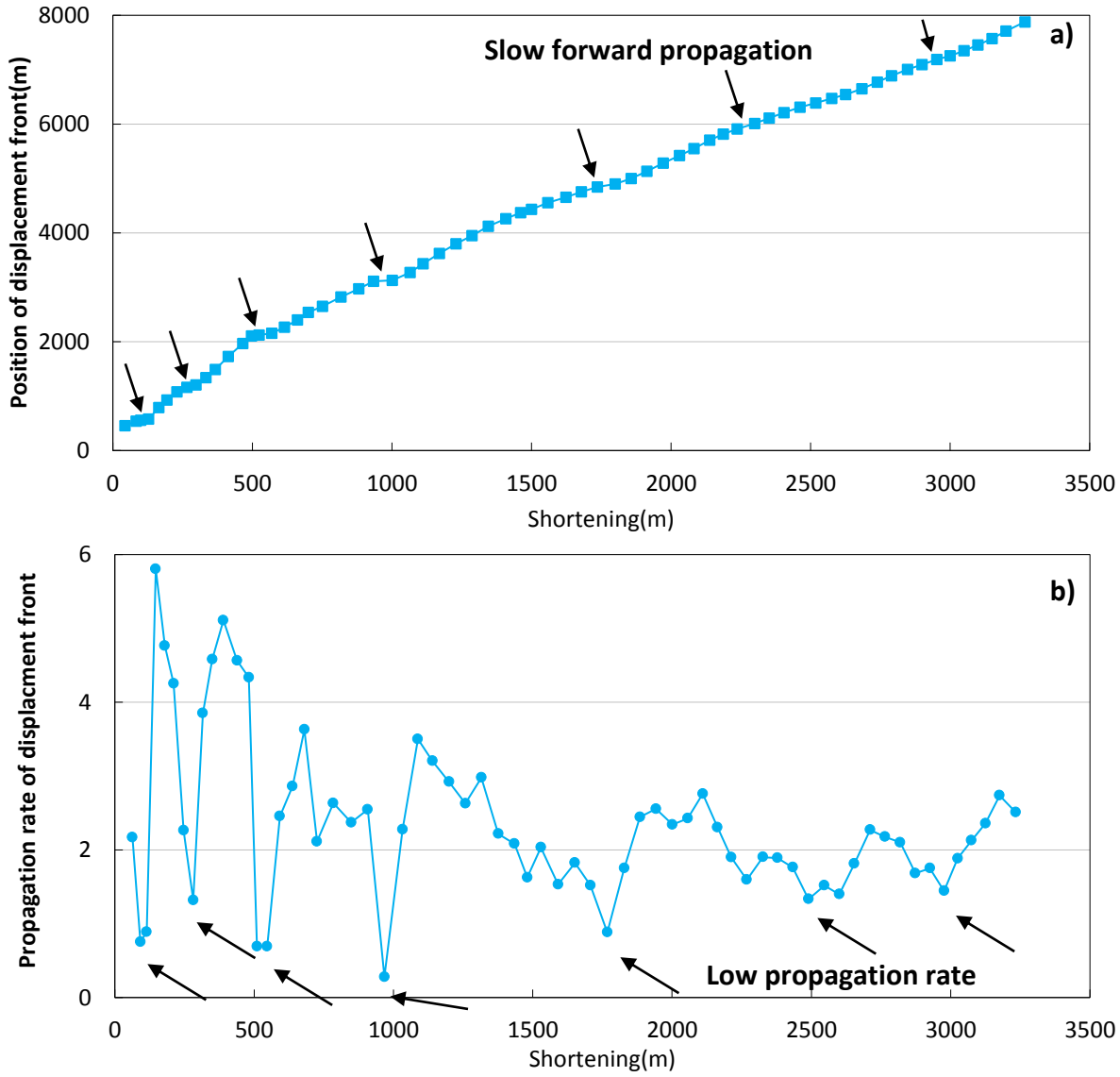
a)
Slow forward propagation
Position of displacement front(m)
8000
6000
4000
2000
0
0
500
1000
1500
2000
2500
3000
3500
Shortening(m)
b)
Propagation rate of displacment front
6
4
2
0
Low propagation rate
0
500
1000
1500
2000
2500
3000
3500
Shortening(m)

Fig. 8.

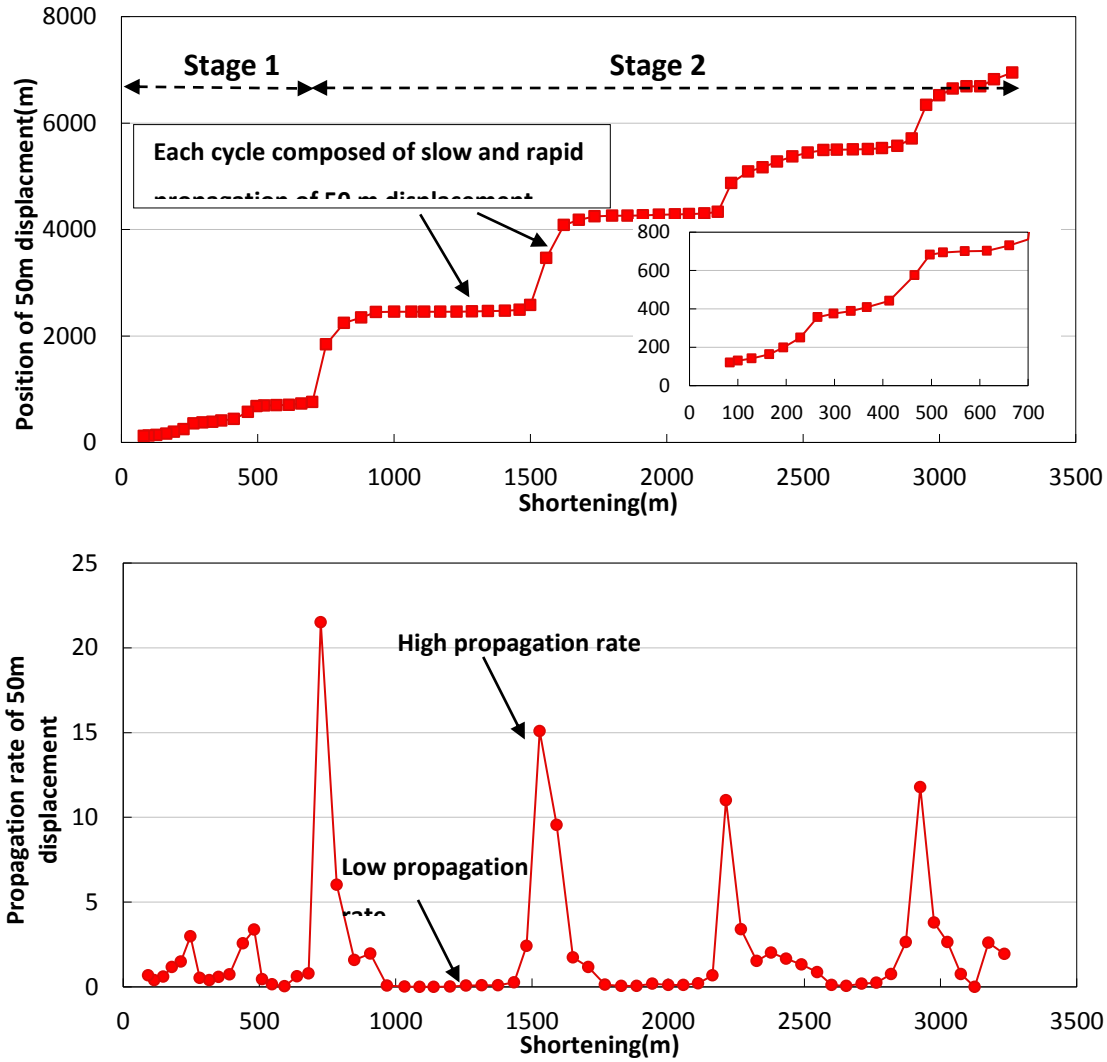
Stage 1
Stage 2
Each cycle composed of slow and rapid
Position of 50m displacment(m)
Shortening(m)
High propagation rate
Low propagation
Propagation rate of 50m displacement
Shortening(m)

Fig. 9.

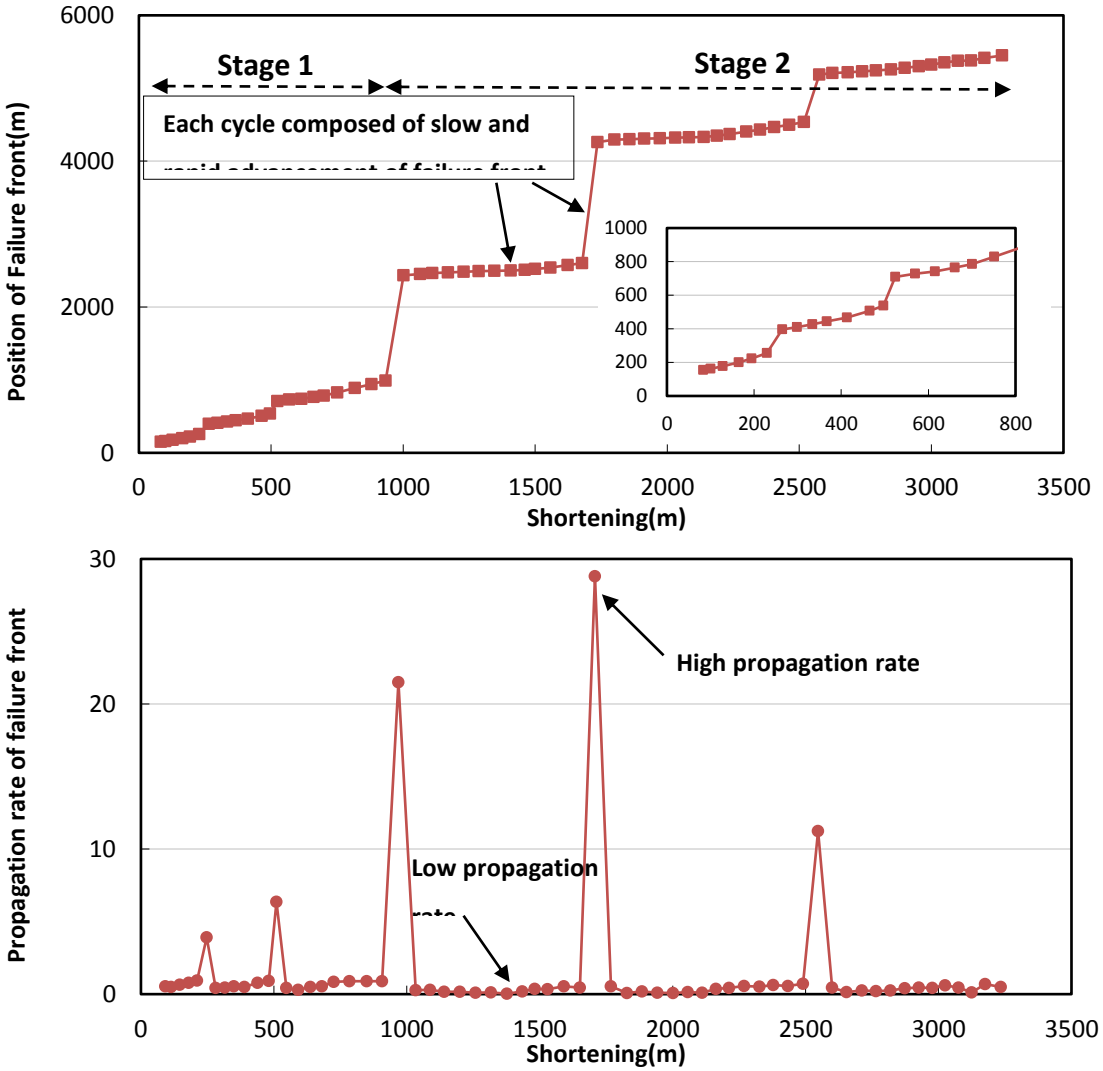
Stage 1
Stage 2
Each cycle composed of slow and
Position of Failure front(m)
Shortening(m)
Propagation rate of failure front
High propagation rate
Low propagation
Shortening(m)

Fig. 10.

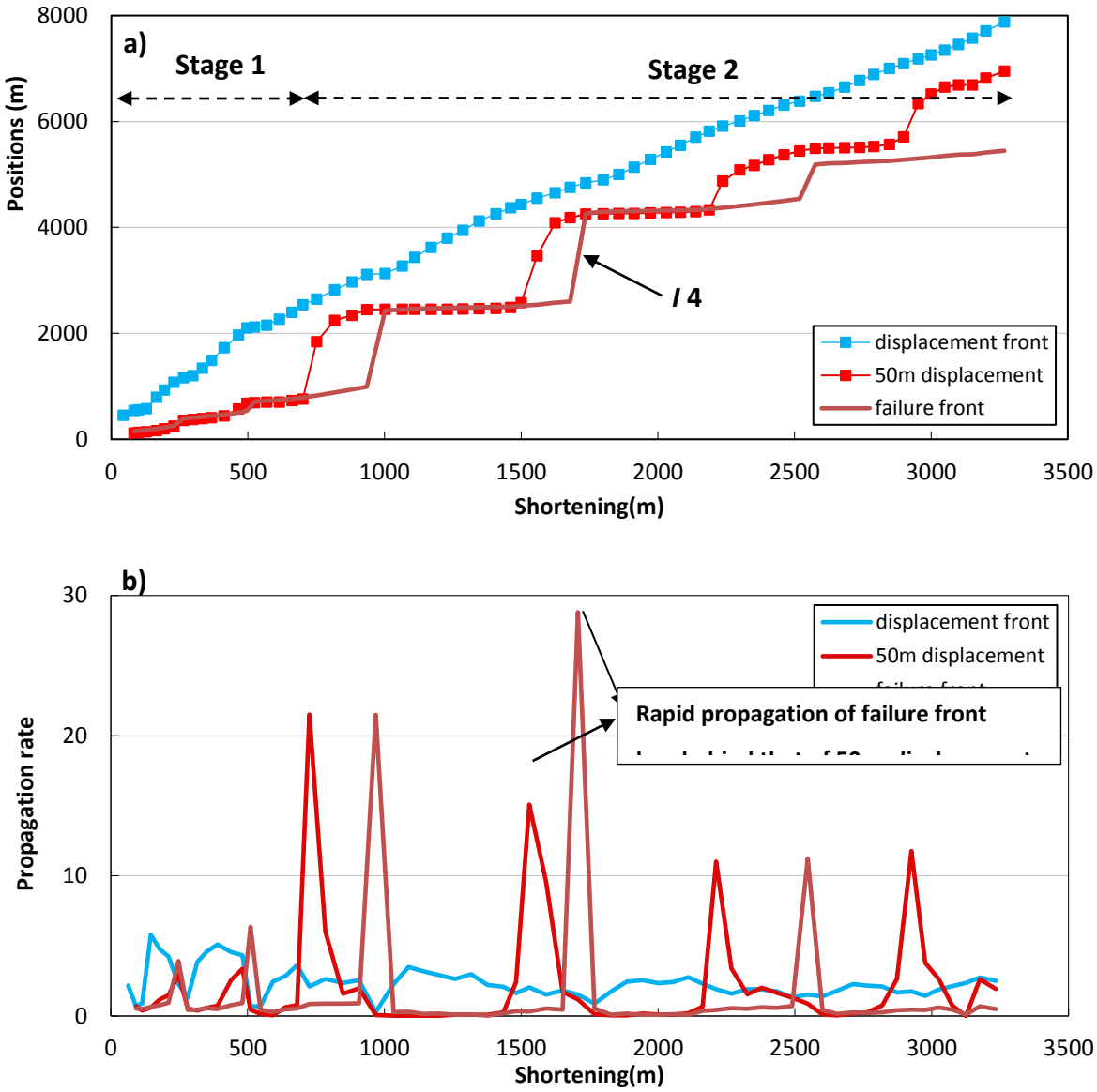
a)
Stage 1
Stage 2
Positions (m)
8000
6000
4000
2000
0
0
500
1000
1500
2000
2500
3000
3500
Shortening(m)
l 4
displacement front
50m displacement
failure front
b)
Propagation rate
30
20
10
0
Rapid propagation of failure front
displacement front
50m displacement

Fig. 11.

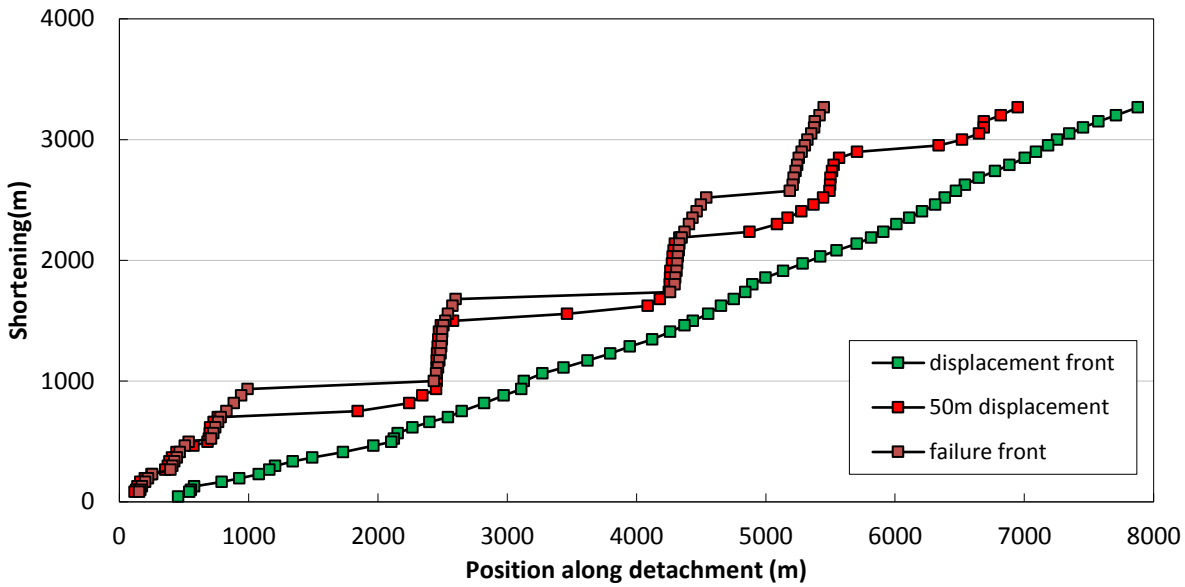
4000
3000
2000
1000
0
Shortening(m)
0
1000
2000
3000
4000
5000
6000
7000
8000
Position along detachment (m)
displacement front
50m displacement
failure front

Fig. 12.

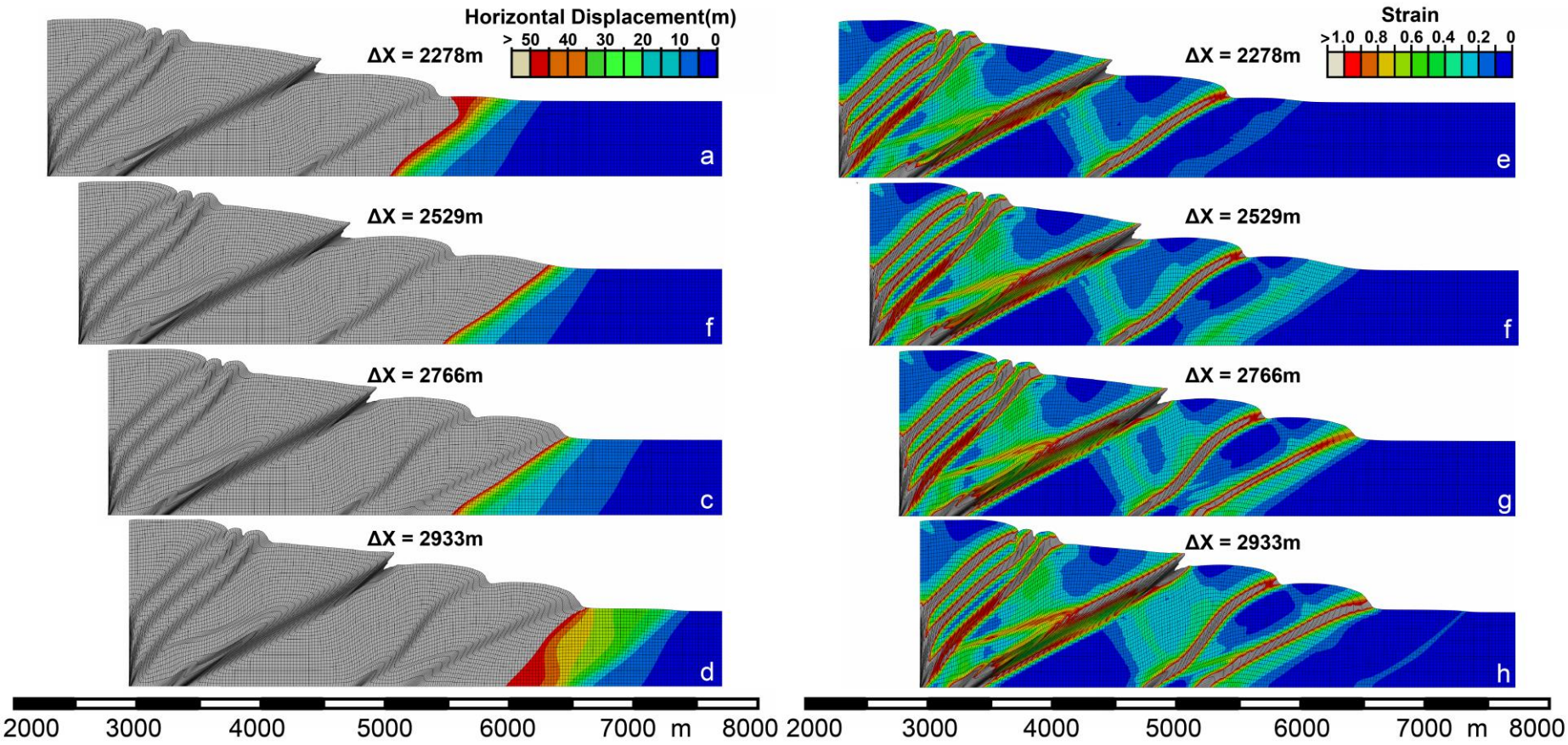
Horizontal Displacement(m)
> 50 40 30 20 10 0
ΔX = 2278m
a
ΔX = 2529m
f
ΔX = 2766m
c
ΔX = 2933m
d
2000 3000 4000 5000 6000 7000 m 8000
Strain
>1.0 0.8 0.6 0.4 0.2 0
ΔX = 2278m
e
ΔX = 2529m
f
ΔX = 2766m
g
ΔX = 2933m
h
2000 3000 4000 5000 6000 7000 m 8000

Fig. 13.

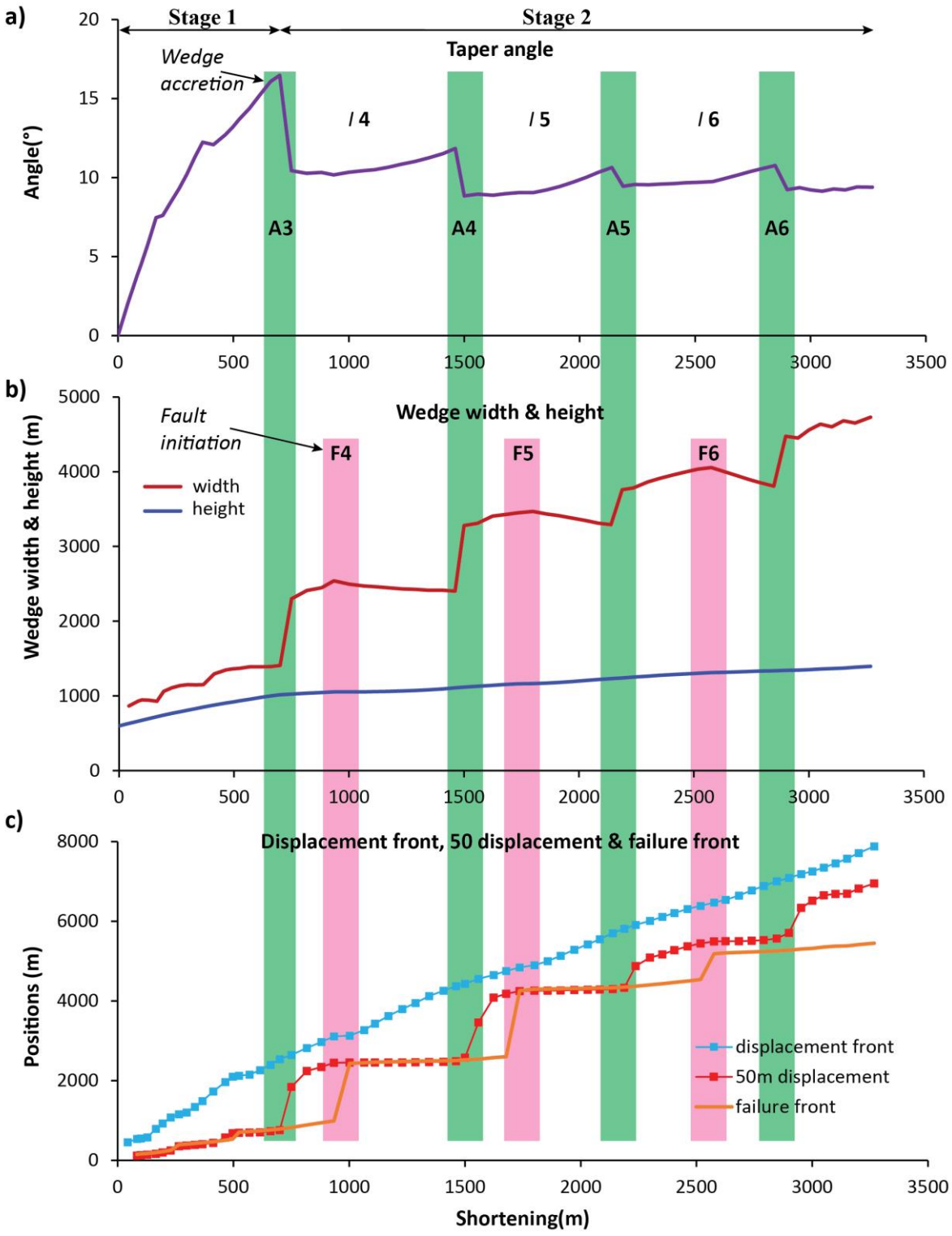
a)
Stage 1
Stage 2
Taper angle
Wedge accretion
/ 4
/ 5
/ 6
A3
A4
A5
A6
Angle(°)
b)
Wedge width & height
Fault initiation
F4
F5
F6
width
height
Wedge width & height (m)
c)
Displacement front, 50 displacement & failure front
displacement front
50m displacement
failure front
Positions (m)
Shortening(m)

Fig. 14.

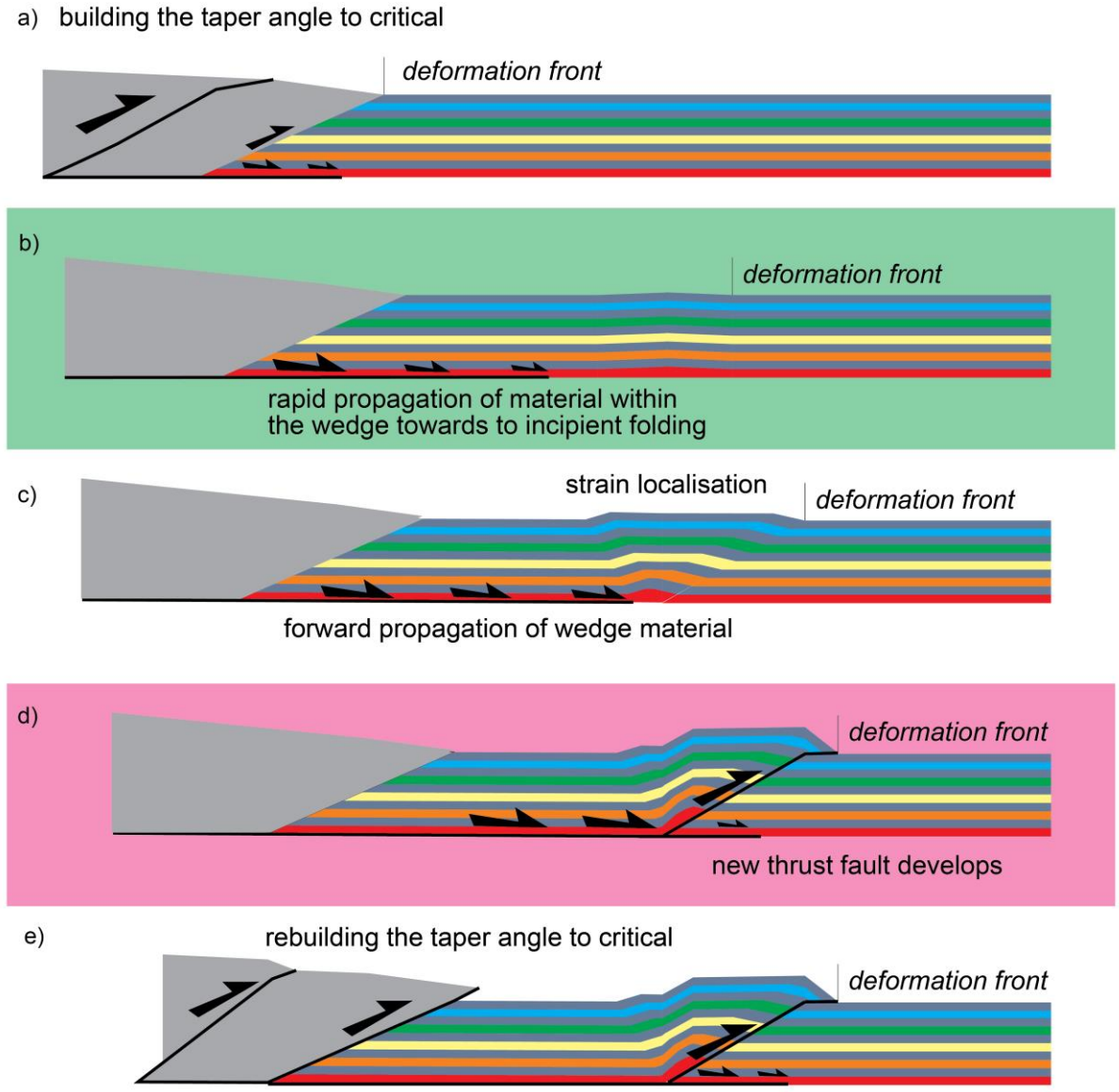
a) building the taper angle to critical
deformation front
b)
deformation front
rapid propagation of material within
the wedge towards to incipient folding
c)
strain localisation
deformation front
forward propagation of wedge material
d)
deformation front
new thrust fault develops
e)
rebuilding the taper angle to critical
deformation front

Fig. 15.